



Differential branching fraction and angular analysis of $\Lambda_b^0 \rightarrow \Lambda \mu^+ \mu^-$ decays

The LHCb collaboration[†]

Abstract

The differential branching fraction of the rare decay $\Lambda_b^0 \rightarrow \Lambda \mu^+ \mu^-$ is measured as a function of q^2 , the square of the dimuon invariant mass. The analysis is performed using proton-proton collision data, corresponding to an integrated luminosity of 3.0 fb^{-1} , collected by the LHCb experiment. Evidence of signal is observed in the q^2 region below the square of the J/ψ mass. Integrating over $15 < q^2 < 20 \text{ GeV}^2/c^4$ the branching fraction is measured as

$$d\mathcal{B}(\Lambda_b^0 \rightarrow \Lambda \mu^+ \mu^-)/dq^2 = (1.18^{+0.09}_{-0.08} \pm 0.03 \pm 0.27) \times 10^{-7} (\text{GeV}^2/c^4)^{-1},$$

where the uncertainties are statistical, systematic and due to the normalisation mode, $\Lambda_b^0 \rightarrow J/\psi \Lambda$, respectively. In the q^2 intervals where the signal is observed, angular distributions are studied and the forward-backward asymmetries in the dimuon (A_{FB}^ℓ) and hadron (A_{FB}^h) systems are measured for the first time. In the range $15 < q^2 < 20 \text{ GeV}^2/c^4$ they are found to be[‡]

$$A_{\text{FB}}^\ell = -0.05 \pm 0.09 (\text{stat}) \pm 0.03 (\text{syst}) \text{ and}$$

$$A_{\text{FB}}^h = -0.29 \pm 0.07 (\text{stat}) \pm 0.03 (\text{syst}).$$

Published in JHEP 06 (2015) 115, JHEP 09 (2018) 145.

© CERN on behalf of the LHCb collaboration, licence CC-BY-4.0.

[†]Authors are listed at the end of this paper.

[‡]Please see erratum in appendix B

1 Introduction

The decay $\Lambda_b^0 \rightarrow \Lambda \mu^+ \mu^-$ is a rare ($b \rightarrow s$) flavour-changing neutral current process that, in the Standard Model (SM), proceeds through electroweak loop (penguin and W^\pm box) diagrams. As non-SM particles may also contribute to the decay amplitudes, measurements of this and similar decays can be used to search for physics beyond the SM. To date, emphasis has been placed on the study of rare decays of mesons rather than baryons, in part due to the theoretical complexity of the latter [1]. In the particular system studied in this analysis, the decay products include only a single long-lived hadron, simplifying the theoretical modelling of hadronic physics in the final state.

The study of Λ_b^0 baryon decays is of considerable interest for several reasons. Firstly, as the Λ_b^0 baryon has non-zero spin, there is the potential to improve the limited understanding of the helicity structure of the underlying Hamiltonian, which cannot be extracted from meson decays [1, 2]. Secondly, as the Λ_b^0 baryon may be considered as consisting of a heavy quark combined with a light diquark system, the hadronic physics differs significantly from that of the B meson decay. A further motivation specific to the $\Lambda_b^0 \rightarrow \Lambda \mu^+ \mu^-$ channel is that the polarisation of the Λ baryon is preserved in the $\Lambda \rightarrow p \pi^-$ decay¹, giving access to complementary information to that available from meson decays [3].

Theoretical aspects of the $\Lambda_b^0 \rightarrow \Lambda \mu^+ \mu^-$ decay have been considered both in the SM and in some of its extensions [3–16]. Although based on the same effective Hamiltonian as that for the corresponding mesonic transitions, the hadronic form factors for the Λ_b^0 baryon case are less well-known due to the less stringent experimental constraints. This leads to a large spread in the predicted branching fractions. The decay has a non-trivial angular structure which, in the case of unpolarised Λ_b^0 production, is described by the helicity angles of the muon and proton, the angle between the planes defined by the Λ decay products and the two muons, and the square of the dimuon invariant mass, q^2 . In theoretical investigations, the differential branching fraction, and forward-backward asymmetries for both the dilepton and the hadron systems of the decay, have received particular attention [3, 11, 15–17]. Different treatments of form factors are used depending on the q^2 region and can be tested by comparing predictions with data as a function of q^2 .

In previous observations of the decay $\Lambda_b^0 \rightarrow \Lambda \mu^+ \mu^-$ [18, 19], evidence for signal had been limited to q^2 values above the square of the mass of the $\psi(2S)$ resonance. This region will be referred to as “high- q^2 ”, while that below the $\psi(2S)$ will be referred to as “low- q^2 ”. In this paper an updated measurement by LHCb of the differential branching fraction for the rare decay $\Lambda_b^0 \rightarrow \Lambda \mu^+ \mu^-$, and the first angular analysis of this decay mode, are reported. Non-overlapping q^2 intervals in the range 0.1–20.0 GeV²/c⁴, and theoretically motivated ranges 1.1–6.0 and 15.0–20.0 GeV²/c⁴ [3, 20, 21], are used. The rates are normalised with respect to the tree-level $b \rightarrow c \bar{c} s$ decay $\Lambda_b^0 \rightarrow J/\psi \Lambda$, where $J/\psi \rightarrow \mu^+ \mu^-$. This analysis uses pp collision data, corresponding to an integrated luminosity of 3.0 fb⁻¹, collected during 2011 and 2012 at centre-of-mass energies of 7 and 8 TeV, respectively.

¹The inclusion of charge-conjugate modes is implicit throughout.

2 Detector and simulation

The LHCb detector [22,23] is a single-arm forward spectrometer covering the pseudorapidity range $2 < \eta < 5$, designed for the study of particles containing b or c quarks. The detector includes a high-precision tracking system (VELO) consisting of a silicon-strip vertex detector surrounding the pp interaction region [24], a large-area silicon-strip detector located upstream of a dipole magnet with a bending power of about 4 Tm, and three stations of silicon-strip detectors and straw drift tubes [25] placed downstream of the magnet. The tracking system provides a measurement of momentum, p , with a relative uncertainty that varies from 0.5% at low momentum to 1.0% at 200 GeV/ c . The minimum distance of a track to a primary vertex, the impact parameter, is measured with a resolution of $(15 + 29/p_T) \mu\text{m}$, where p_T is the component of the momentum transverse to the beam, in GeV/ c . Different types of charged hadrons are distinguished using information from two ring-imaging Cherenkov (RICH) detectors [26]. Photon, electron and hadron candidates are identified using a calorimeter system that consists of scintillating-pad and preshower detectors, an electromagnetic calorimeter and a hadronic calorimeter. Muons are identified by a system composed of alternating layers of iron and multiwire proportional chambers [27].

The trigger [28] consists of a hardware stage, based on information from the calorimeter and muon systems, followed by a software stage in which a full event reconstruction is carried out. Candidate events are first required to pass a hardware trigger, which selects muons with a transverse momentum $p_T > 1.48$ GeV/ c in the 7 TeV data or $p_T > 1.76$ GeV/ c in the 8 TeV data. In the subsequent software trigger, at least one of the final-state charged particles is required to have both $p_T > 0.8$ GeV/ c and impact parameter greater than 100 μm with respect to all of the primary pp interaction vertices (PVs) in the event. Finally, the tracks of two or more of the final-state particles are required to form a vertex that is significantly displaced from the PVs.

Simulated samples of pp collisions are generated using PYTHIA [29] with a specific LHCb configuration [30]. Decays of hadronic particles are described by EVTGEN [31], in which final-state radiation is generated using PHOTOS [32]. The interaction of the generated particles with the detector, and its response, are implemented using the GEANT4 toolkit [33] as described in Ref. [34]. The model used in the simulation of $\Lambda_b^0 \rightarrow \Lambda \mu^+ \mu^-$ decays includes q^2 and angular dependence as described in Ref. [16], together with Wilson coefficients based on Refs. [35,36]. Interference effects from J/ψ and $\psi(2S)$ contributions are not included. For the $\Lambda_b^0 \rightarrow J/\psi \Lambda$ decay the simulation model is based on the angular distributions observed in Ref. [37].

3 Candidate selection

Candidate $\Lambda_b^0 \rightarrow \Lambda \mu^+ \mu^-$ (signal mode) and $\Lambda_b^0 \rightarrow J/\psi \Lambda$ (normalisation mode) decays are reconstructed from a Λ baryon candidate and either a dimuon or a J/ψ meson candidate, respectively. The $\Lambda_b^0 \rightarrow J/\psi \Lambda$ mode, with the J/ψ meson reconstructed via its dimuon decay, is a convenient normalisation process because it has the same final-state particles

as the signal mode. Signal and normalisation channels are distinguished by the q^2 interval in which they fall.

The dimuon candidates are formed from two well-reconstructed oppositely charged particles that are significantly displaced from any PV, identified as muons and consistent with originating from a common vertex.

Candidate Λ decays are reconstructed in the $\Lambda \rightarrow p\pi^-$ mode from two oppositely charged tracks that either both include information from the VELO (*long* candidates), or both do not include information from the VELO (*downstream* candidates). The Λ candidates must also have a vertex fit with a good χ^2 , a decay time of at least 2 ps and an invariant mass within $30 \text{ MeV}/c^2$ of the known Λ mass [38]. For long candidates, charged particles must have $p_T > 0.25 \text{ GeV}/c$ and a further requirement is imposed on the particle identification (PID) of the proton using a likelihood variable that combines information from the RICH detectors and the calorimeters.

Candidate Λ_b^0 decays are formed from Λ and dimuon candidates that have a combined invariant mass in the interval $5.3\text{--}7.0 \text{ GeV}/c^2$ and form a good-quality vertex that is well-separated from any PV. Candidates pointing to the PV with which they are associated are selected by requiring that the angle between the Λ_b^0 momentum vector and the vector between the PV and the Λ_b^0 decay vertex, θ_D , is less than 14 mrad. After the Λ_b^0 candidate is built, a kinematic fit [39] of the complete decay chain is performed in which the proton and pion are constrained such that the $p\pi^-$ invariant mass corresponds to the known Λ baryon mass, and the Λ and dimuon systems are constrained to originate from their respective vertices. Furthermore, candidates falling in the $8 - 11$ and $12.5 - 15 \text{ GeV}^2/c^4$ q^2 intervals are excluded from the rare sample as they are dominated by decays via J/ψ and $\psi(2S)$ resonances.

The final selection is based on a neural network classifier [40, 41], exploiting 15 variables carrying kinematic, candidate quality and particle identification information. Both the track parameter resolutions and kinematic properties are different for downstream and long Λ decays and therefore a separate training is performed for each category. The signal sample used to train the neural network consists of simulated $\Lambda_b^0 \rightarrow \Lambda\mu^+\mu^-$ events, while the background is taken from data in the upper sideband of the Λ_b^0 candidate mass spectrum, between 6.0 and $7.0 \text{ GeV}/c^2$. Candidates with a dimuon mass in either the J/ψ or $\psi(2S)$ regions ($\pm 100 \text{ MeV}/c^2$ intervals around their known masses) are excluded from the training samples. The variable that provides the greatest discrimination in the case of long candidates is the χ^2 from the kinematic fit. For downstream candidates, the p_T of the Λ candidate is the most powerful variable. Other variables that contribute significantly are: the PID information for muons; the separation of the muons, the pion and the Λ_b^0 candidate from the PV; the distance between the Λ and Λ_b^0 decay vertices; and the pointing angle, θ_D .

The requirement on the response of the neural network classifier is chosen separately for low- and high- q^2 candidates using two different figures of merit. In the low- q^2 region, where the signal has not been previously established, the figure of merit $\varepsilon/(\sqrt{N_B} + a/2)$ [42] is used, where ε and N_B are the signal efficiency and the expected number of background decays and a is the target significance; a value of $a = 3$ is used. In contrast, for the

high- q^2 region the figure of merit $N_S/\sqrt{N_S + N_B}$ is maximised, where N_S is the expected number of signal candidates. To ensure an appropriate normalisation of N_S , the number of $\Lambda_b^0 \rightarrow J/\psi \Lambda$ candidates that satisfy the preselection is scaled by the measured ratio of branching fractions of $\Lambda_b^0 \rightarrow \Lambda \mu^+ \mu^-$ to $\Lambda_b^0 \rightarrow J/\psi (\rightarrow \mu^+ \mu^-) \Lambda$ decays [19], and the $J/\psi \rightarrow \mu^+ \mu^-$ branching fraction [38]. The value of N_B is determined by extrapolating the number of candidate decays found in the background training sample into the signal region. Relative to the preselected event sample, the neural network retains approximately 96 % (66 %) of downstream candidates and 97 % (82 %) of long candidates for the selection at high (low) q^2 .

4 Peaking backgrounds

In addition to combinatorial background formed from the random combination of particles, backgrounds due to specific decays are studied using fully reconstructed samples of simulated b hadron decays in which the final state includes two muons. For the $\Lambda_b^0 \rightarrow J/\psi \Lambda$ channel, the only significant contribution is from $B^0 \rightarrow J/\psi K_s^0$ decays, with $K_s^0 \rightarrow \pi^+ \pi^-$ where one of the pions is misidentified as a proton. This decay contains a long-lived K_s^0 meson and therefore has the same topology as the $\Lambda_b^0 \rightarrow J/\psi \Lambda$ mode. This contribution leads to a broad shape that peaks below the Λ_b^0 mass region, which is taken into account in the mass fit.

For the $\Lambda_b^0 \rightarrow \Lambda \mu^+ \mu^-$ channel two sources of peaking background are identified. The first of these is $\Lambda_b^0 \rightarrow J/\psi \Lambda$ decays in which an energetic photon is radiated from either of the muons; this constitutes a background in the q^2 region just below the square of the J/ψ mass and in a mass region significantly below the Λ_b^0 mass. These events do not contribute significantly in the q^2 intervals chosen for the analysis. The second source of background is due to $B^0 \rightarrow K_s^0 \mu^+ \mu^-$ decays, where $K_s^0 \rightarrow \pi^+ \pi^-$ and one of the pions is misidentified as a proton. This contribution is estimated by scaling the number of $B^0 \rightarrow J/\psi K_s^0$ events found in the $\Lambda_b^0 \rightarrow J/\psi \Lambda$ fit by the ratio of the world average branching fractions for the decay processes $B^0 \rightarrow K_s^0 \mu^+ \mu^-$ and $B^0 \rightarrow J/\psi (\rightarrow \mu^+ \mu^-) K_s^0$ [38]. Integrated over q^2 this is estimated to yield fewer than ten events, which is small relative to the expected total background level.

5 Yields

5.1 Fit procedure

The yields of signal and background events in the data are determined in the mass range 5.35–6.00 GeV/ c^2 using unbinned extended maximum likelihood fits for the $\Lambda_b^0 \rightarrow \Lambda \mu^+ \mu^-$ and the $\Lambda_b^0 \rightarrow J/\psi \Lambda$ modes. The likelihood function has the form

$$\mathcal{L} = e^{-(N_S + N_C + N_P)} \times \prod_{i=1}^N [N_S P_S(m_i) + N_C P_C(m_i) + N_P P_P(m_i)], \quad (1)$$

where N_S , N_C and N_P are the number of signal, combinatorial and peaking background events, respectively, $P_j(m_i)$ are the corresponding probability density functions (PDFs) and m_i is the mass of the Λ_b^0 candidate. The signal yield itself is parametrised in the fit using the relative branching fraction of the signal and normalisation modes,

$$N_S(\Lambda\mu^+\mu^-)_k = \left[\frac{d\mathcal{B}(\Lambda\mu^+\mu^-)/dq^2}{\mathcal{B}(J/\psi\Lambda)} \right] \cdot N_S(J/\psi\Lambda)_k \cdot \varepsilon_k^{\text{rel}} \cdot \frac{\Delta q^2}{\mathcal{B}(J/\psi \rightarrow \mu^+\mu^-)}, \quad (2)$$

where k is the candidate category (long or downstream), Δq^2 is the width of the q^2 interval considered and $\varepsilon_k^{\text{rel}}$ is the relative efficiency, fixed to the values obtained as described in Sec. 6. Fitting the ratio of the branching fractions of signal and normalisation modes simultaneously in both candidate categories makes better statistical use of the data.

The signal shape, in both $\Lambda_b^0 \rightarrow \Lambda\mu^+\mu^-$ and $\Lambda_b^0 \rightarrow J/\psi\Lambda$ modes, is described by the sum of two Crystal Ball functions [43] that share common means and tail parameters but have independent widths. The combinatorial background is parametrised by an exponential function, independently in each q^2 interval. The background due to $B^0 \rightarrow J/\psi K_S^0$ decays is modelled by the sum of two Crystal Ball functions with opposite tails. All shape parameters are independent for the downstream and long sample.

For the $\Lambda_b^0 \rightarrow J/\psi\Lambda$ mode, the widths and common mean in the signal parametrisation are free parameters. The parameters describing the shape of the peaking background are fixed to those derived from simulated $B^0 \rightarrow J/\psi K_S^0$ decays, with only the normalisation allowed to vary to accommodate differences between data and simulation.

For the $\Lambda_b^0 \rightarrow \Lambda\mu^+\mu^-$ decay, the signal shape parameters are fixed according to the result of the fit to $\Lambda_b^0 \rightarrow J/\psi\Lambda$ data and the widths are rescaled to allow for possible differences in resolution as a function of q^2 . The scaling factor is determined comparing $\Lambda_b^0 \rightarrow J/\psi\Lambda$ and $\Lambda_b^0 \rightarrow \Lambda\mu^+\mu^-$ simulated events. The $B^0 \rightarrow K_S^0\mu^+\mu^-$ background component is also modelled using the sum of two Crystal Ball functions with opposite tails where both the yield and all shape parameters are constrained to those obtained from simulated events.

5.2 Fit results

The invariant mass distribution of the $\Lambda_b^0 \rightarrow J/\psi\Lambda$ candidates selected with the high- q^2 requirements is shown in Fig. 1, combining both long and downstream candidates. The normalisation channel candidates are divided into four sub-samples: downstream and long events are fitted separately and each sample is selected with both the low- q^2 and high- q^2 requirements to normalise the corresponding q^2 regions in signal. The number of $\Lambda_b^0 \rightarrow J/\psi\Lambda$ decays found in each case is given in Table 1.

The fraction of peaking background events is larger in the downstream sample amounting to 28 % of the $\Lambda_b^0 \rightarrow J/\psi\Lambda$ yield in the full fitted mass range, while in the sample of long candidates it constitutes about 4 %.

The invariant mass distributions for the $\Lambda_b^0 \rightarrow \Lambda\mu^+\mu^-$ process, integrated over $15.0 < q^2 < 20.0 \text{ GeV}^2/c^4$ and in eight separate q^2 intervals, are shown in Figs. 2 and 3. The yields found in each q^2 interval are given in Table 2 together with their significances. The statistical significance of the observed signal yields is evaluated as $\sqrt{2\Delta \ln \mathcal{L}}$, where $\Delta \ln \mathcal{L}$

Table 1: Number of $\Lambda_b^0 \rightarrow J/\psi \Lambda$ decays in the long and downstream categories found using the selection for low- and high- q^2 regions. Uncertainties shown are statistical only.

Selection	N_S (long)	N_S (downstream)
high- q^2	4313 ± 70	$11\,497 \pm 123$
low- q^2	3363 ± 59	7225 ± 89

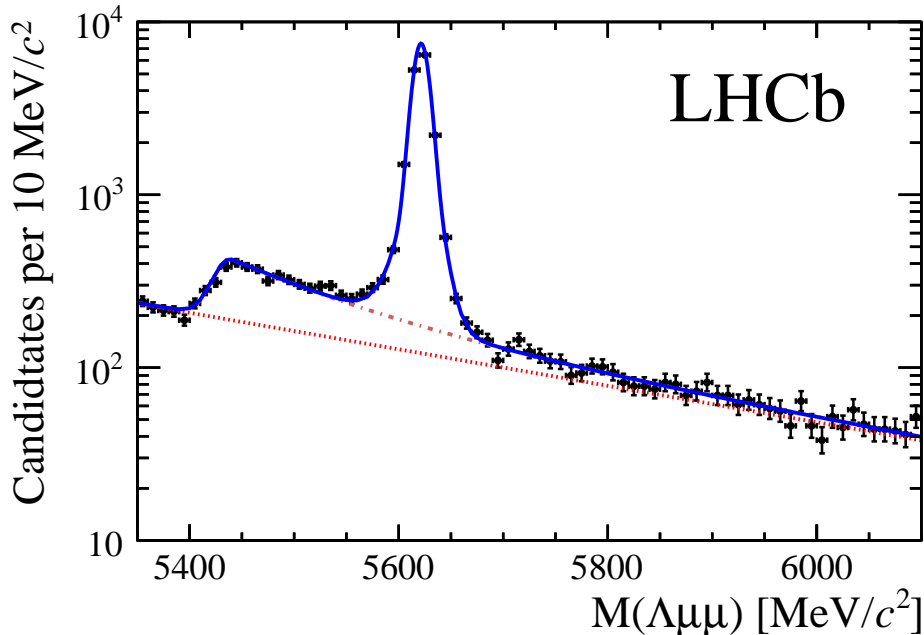


Figure 1: Invariant mass distribution of the $\Lambda_b^0 \rightarrow J/\psi \Lambda$ candidates selected with the neural network requirement used for the high- q^2 region. The (black) points show data, combining downstream and long candidates, and the solid (blue) line represents the overall fit function. The dotted (red) line represents the combinatorial and the dash-dotted (brown) line the peaking background from $B^0 \rightarrow J/\psi K_s^0$ decays.

is the change in the logarithm of the likelihood function when the signal component is excluded from the fit, relative to the nominal fit in which it is present.

6 Relative efficiency

The measurement of the differential branching fraction of $\Lambda_b^0 \rightarrow \Lambda \mu^+ \mu^-$ relative to $\Lambda_b^0 \rightarrow J/\psi \Lambda$ benefits from the cancellation of several potential sources of systematic uncertainty in the ratio of efficiencies, $\varepsilon^{\text{rel}} = \varepsilon_{\text{tot}}(\Lambda_b^0 \rightarrow \Lambda \mu^+ \mu^-) / \varepsilon_{\text{tot}}(\Lambda_b^0 \rightarrow J/\psi \Lambda)$. Due to the long lifetime of Λ baryons, most of the candidates are reconstructed in the downstream category, with an overall efficiency of 0.20%, while the typical efficiency is 0.05% for long candidates.

The efficiency of the PID is obtained from a data-driven method [26] and found to

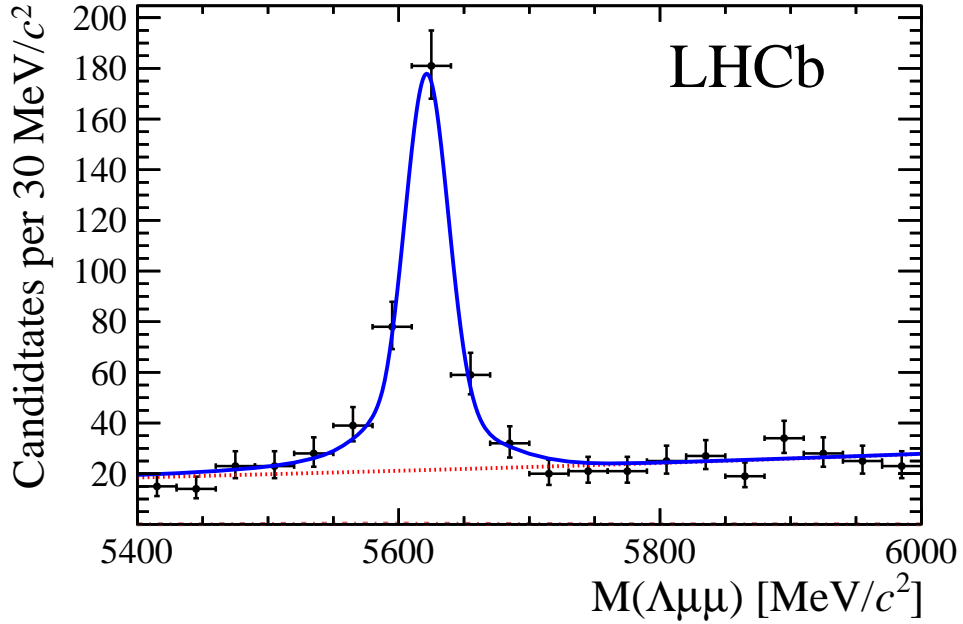


Figure 2: Invariant mass distribution of the $\Lambda_b^0 \rightarrow \Lambda \mu^+ \mu^-$ candidates, integrated over the region $15.0 < q^2 < 20.0 \text{ GeV}^2/c^4$ together with the fit function described in the text. The points show data, the solid (blue) line is the overall fit function and the dotted (red) line represents the combinatorial background. The background component from $B^0 \rightarrow K_S^0 \mu^+ \mu^-$ decays, (brown) dashed line, is barely visible due to the very low yield.

Table 2: Signal decay yields (N_S) obtained from the mass fit to $\Lambda_b^0 \rightarrow \Lambda \mu^+ \mu^-$ candidates in each q^2 interval together with their statistical significances. The yields are the sum of long and downstream categories with downstream decays comprising $\sim 80\%$ of the total yield. The $8 - 11$ and $12.5 - 15 \text{ GeV}^2/c^4$ q^2 intervals are excluded from the study as they are dominated by decays via charmonium resonances.

q^2 interval [GeV^2/c^4]	Total signal yield	Significance
0.1 – 2.0	16.0 ± 5.3	4.4
2.0 – 4.0	4.8 ± 4.7	1.2
4.0 – 6.0	0.9 ± 2.3	0.5
6.0 – 8.0	11.4 ± 5.3	2.7
11.0 – 12.5	60 ± 12	6.5
15.0 – 16.0	57 ± 9	8.7
16.0 – 18.0	118 ± 13	13
18.0 – 20.0	100 ± 11	14
1.1 – 6.0	9.4 ± 6.3	1.7
15.0 – 20.0	276 ± 20	21

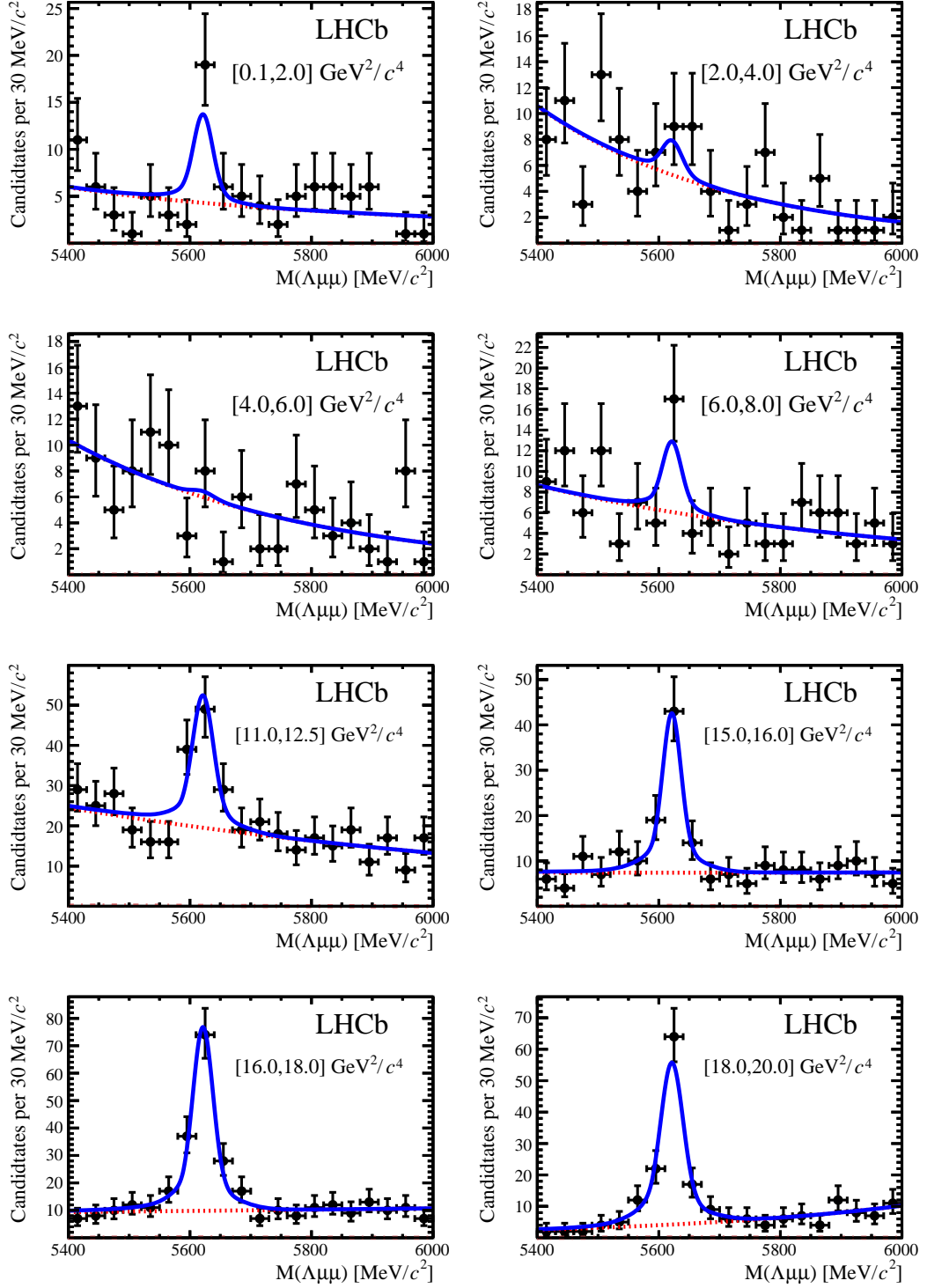


Figure 3: Invariant mass distributions of $\Lambda_b^0 \rightarrow \Lambda \mu^+ \mu^-$ candidates, in eight q^2 intervals, together with the fit function described in the text. The points show data, the solid (blue) line is the overall fit function and the dotted (red) line represents the combinatorial background component.

be 98 % while all other efficiencies are evaluated using simulated data. The models used for the simulation are summarised in Sec. 2. The trigger efficiency is calculated using simulated data and increases from approximately 56 % to 86 % between the lowest and highest q^2 regions. An independent cross-check of the trigger efficiency is performed using a data-driven method. This exploits the possibility of categorising a candidate $\Lambda_b^0 \rightarrow \Lambda \mu^+ \mu^-$ or $\Lambda_b^0 \rightarrow J/\psi \Lambda$ decay in two ways depending on which tracks are directly responsible for its selection by the trigger: “trigger on signal” candidates, where the tracks responsible for the hardware and software trigger decisions are associated with the signal; and “trigger independent of signal” candidates, with a Λ_b^0 baryon reconstructed in either of these channels but where the trigger decision does not depend on any of their decay products. As these two categories of event are not mutually exclusive, their overlap may be used to estimate the efficiency of the trigger selection using data. Using $\Lambda_b^0 \rightarrow J/\psi \Lambda$ candidates and calculating the ratio of yields that are classified as both trigger on signal and independent of signal, relative to those that are classified as trigger independent of signal, an efficiency of $(70 \pm 5) \%$ is obtained, which is consistent with that of $(73.33 \pm 0.02) \%$ computed from simulation.

The relative efficiency for the ratio of branching fractions in each q^2 interval, calculated from the absolute efficiencies described above, is shown in Fig. 4. The increase in efficiency as a function of increasing q^2 is dominated by two effects. Firstly, at low q^2 the muons have lower momenta and therefore have a lower probability of satisfying the trigger requirements. Secondly, at low q^2 the Λ baryon has a larger fraction of the Λ_b^0 momentum and is more likely to decay outside of the acceptance of the detector. Separate selections are used for the low- and high- q^2 regions and, as can be seen in Fig. 4, the tighter neural network requirement used in the low- q^2 region has a stronger effect on downstream candidates.

The uncertainties combine both statistical and systematic contributions (with the latter dominating) and include a small correlated uncertainty due to the use of a single simulated sample of $\Lambda_b^0 \rightarrow J/\psi \Lambda$ decays as the normalisation channel for all q^2 intervals. Systematic uncertainties associated with the efficiency calculation are described in detail in Sec. 7.

7 Systematic uncertainties on the branching fraction

7.1 Yields

Three sources of systematic uncertainty on the measured yields are considered for both the $\Lambda_b^0 \rightarrow J/\psi \Lambda$ and the $\Lambda_b^0 \rightarrow \Lambda \mu^+ \mu^-$ decay modes: the shape of the signal PDF, the shape of the background PDF and the choice of the fixed parameters used in the fits to data.

For both decays, the default signal PDF is replaced by the sum of two Gaussian functions. All parameters of the Gaussian functions are allowed to vary to take into account the effect of fixing parameters. The shape of the background function is changed by permitting the $K_s^0 \mu^+ \mu^-$ peaking background yield, which is fixed to the value obtained from simulation the nominal fit, to vary. For the resonant channel, the $J/\psi K_s^0$ peaking background shape is changed by fixing the global shift to zero. Finally, simulated experiments are performed

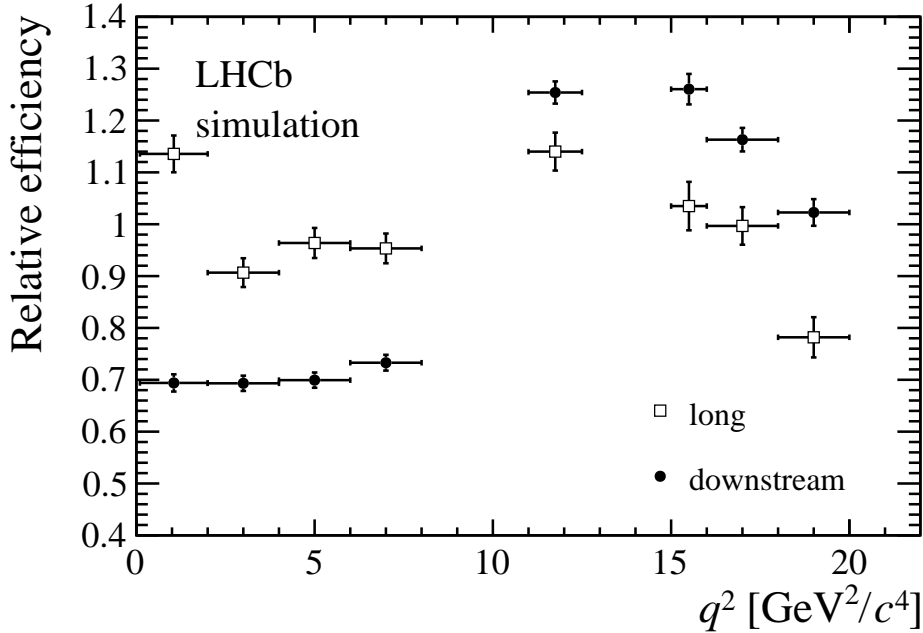


Figure 4: Total relative efficiency, ε_{rel} , between $\Lambda_b^0 \rightarrow \Lambda \mu^+ \mu^-$ and $\Lambda_b^0 \rightarrow J/\psi \Lambda$ decays. The uncertainties are the combination of both statistical and systematic components, and are dominated by the latter.

using the default model, separately for each q^2 interval, generating the same number of events as observed in data. Each distribution is fitted with the default model and the modified PDFs. The average deviation over the ensemble of simulated experiments is assigned as the systematic uncertainty. The relative change in signal yield due to the choice of signal PDF varies between 0.6 % and 4.6 % depending on q^2 , while the change due to the choice of background PDF is in the range between 1.1 % and 2.5 %. The q^2 intervals that are most affected are those in which a smaller number of candidates is observed and therefore there are fewer constraints to restrict potentially different PDFs. The systematic uncertainties on the yield in each q^2 interval are summarised in Table 3, where the total is the sum in quadrature of the individual components.

7.2 Relative efficiencies

The dominant systematic effect is that related to the current knowledge of the angular structure and the q^2 dependence of the decay channels. The uncertainty due to the finite size of simulated samples is comparable to that from other sources. The total systematic uncertainties on the efficiencies, calculated as the sums in quadrature of the individual components described below, are summarised in Table 3.

7.2.1 Decay structure and production polarisation

The main factors that affect the detection efficiencies are the angular structure of the decays and the production polarisation (P_b). Although these arise from different parts of the process, the efficiencies are linked and are therefore treated together.

For the $\Lambda_b^0 \rightarrow \Lambda \mu^+ \mu^-$ decay, the impact of the limited knowledge of the production polarisation, P_b , is estimated by comparing the default efficiency, obtained in the unpolarised scenario, with those in which the polarisation is varied within its measured uncertainties, using the most recent LHCb measurement, $P_b = 0.06 \pm 0.09$ [37]. The larger of these differences is assigned as the systematic uncertainty from this source. This yields a $\sim 0.5\%$ uncertainty on the efficiency of downstream candidates and $\sim 1.2\%$ for long candidates. No significant q^2 dependence is found.

To assess the systematic uncertainty due to the limited knowledge of the decay structure, the efficiency corresponding to the default model [16, 35, 44] is compared to that of a model containing an alternative set of form factors based on a lattice QCD calculation [15]. The larger of the full difference or the statistical precision is assigned as the systematic uncertainty.

For the $\Lambda_b^0 \rightarrow J/\psi \Lambda$ mode, the default angular distribution is based on that observed in Ref. [37]. The angular distribution is determined by the production polarisation and four complex decay amplitudes. The central values from Ref. [37] are used for the nominal result. To assess the sensitivity of the $\Lambda_b^0 \rightarrow J/\psi \Lambda$ mode to the choice of decay model, the production polarisation and decay amplitudes are varied within their uncertainties, taking into account correlations.

To assess the potential impact that physics beyond the SM might have on the detection efficiency, the C_7 and C_9 Wilson coefficients are modified by adding a non-SM contribution ($C_i \rightarrow C_i + C'_i$). The C'_i added are inspired to maintain compatibility with the recent LHCb result for the P'_5 observable [45] and indicate a change at the level of $\sim 7\%$ in the 0.1–2.0 q^2 interval, and 2–3% in other regions. No systematic is assigned as a result of this study.

7.2.2 Reconstruction efficiency for the Λ baryon

The Λ baryon is reconstructed from either long or downstream tracks, and their relative proportions differ in data and simulation. This proportion does not depend significantly on q^2 and therefore possible effects cancel in the ratio with the normalisation channel. Furthermore, since the analysis is performed separately for long and downstream candidates, it is not necessary to assign a systematic uncertainty to account for a potential effect due to the different fractions of candidates of the two categories observed in data and simulation. To allow for residual differences between data and simulation that do not cancel completely in the ratio between signal and normalisation modes, systematic uncertainties of 0.8% and 1.2% are estimated for the low- q^2 and high- q^2 regions, respectively, using the same data-driven method as in Ref. [46].

Table 3: Systematic uncertainties as a function of q^2 , assigned for yields and efficiencies. Values reported are the sums in quadrature of all contributions evaluated within each category.

q^2 interval [GeV ² /c ⁴]	Syst. on yields [%]	Syst. on eff. [%]
0.1 – 2.0	3.4	+2.2 –3.6
2.0 – 4.0	3.8	+2.2 –4.1
4.0 – 6.0	6.6	+17.2 –14.3
6.0 – 8.0	2.0	+2.1 –3.1
11.0 – 12.5	3.2	+3.7 –5.2
15.0 – 16.0	2.8	+3.1 –2.8
16.0 – 18.0	1.4	+3.0 –4.1
18.0 – 20.0	2.5	+3.9 –2.3
1.1 – 6.0	4.2	+2.2 –4.6
15.0 – 20.0	1.0	+2.0 –2.9

7.2.3 Production kinematics and lifetime of the Λ_b^0 baryon

In $\Lambda_b^0 \rightarrow J/\psi \Lambda$ decays a small difference is observed between data and simulation in the momentum and transverse momentum distributions of the Λ_b^0 baryon produced. Simulated data are reweighted to reproduce these distributions in data and the relative efficiencies are compared to those obtained using events that are not reweighted. This effect is less than 0.1 %, which is negligible with respect to other sources.

Finally, the Λ_b^0 baryon lifetime used throughout corresponds to the most recent LHCb measurement, 1.479 ± 0.019 ps [47]. The associated systematic uncertainty is estimated by varying the lifetime value by one standard deviation and negligible differences are found.

8 Differential branching fraction

The values for the absolute branching fraction of the $\Lambda_b^0 \rightarrow \Lambda \mu^+ \mu^-$ decay, obtained by multiplying the relative branching fraction by the absolute branching fraction of the normalisation channel, $\mathcal{B}(\Lambda_b^0 \rightarrow J/\psi \Lambda) = (6.3 \pm 1.3) \times 10^{-4}$ [38], are given in Fig. 5 and summarised in Table 4, where the SM predictions are obtained from Ref. [15]. The relative branching fractions are given in the Appendix.

Evidence for signal is found in the q^2 region between the charmonium resonances and in the interval $0.1 < q^2 < 2.0$ GeV²/c⁴, where an increased yield is expected due to the proximity of the photon pole. The uncertainty on the branching fraction is dominated by the precision of the branching fraction for the normalisation channel, while the uncertainty on the relative branching fraction is dominated by the size of the data sample available. The data are consistent with the theoretical predictions in the high- q^2 region but lie below

the predictions in the low- q^2 region.

Table 4: Measured differential branching fraction of $\Lambda_b^0 \rightarrow \Lambda \mu^+ \mu^-$, where the uncertainties are statistical, systematic and due to the uncertainty on the normalisation mode, $\Lambda_b^0 \rightarrow J/\psi \Lambda$, respectively.

q^2 interval [GeV $^2/c^4$]	$d\mathcal{B}(\Lambda_b^0 \rightarrow \Lambda \mu^+ \mu^-)/dq^2 \cdot 10^{-7}[(\text{GeV}^2/c^4)^{-1}]$			
0.1 – 2.0	0.36	+0.12 -0.11	+0.02 -0.02	± 0.07
2.0 – 4.0	0.11	+0.12 -0.09	+0.01 -0.01	± 0.02
4.0 – 6.0	0.02	+0.09 -0.00	+0.01 -0.01	± 0.01
6.0 – 8.0	0.25	+0.12 -0.11	+0.01 -0.01	± 0.05
11.0 – 12.5	0.75	+0.15 -0.14	+0.03 -0.05	± 0.15
15.0 – 16.0	1.12	+0.19 -0.18	+0.05 -0.05	± 0.23
16.0 – 18.0	1.22	+0.14 -0.14	+0.03 -0.06	± 0.25
18.0 – 20.0	1.24	+0.14 -0.14	+0.06 -0.05	± 0.26
1.1 – 6.0	0.09	+0.06 -0.05	+0.01 -0.01	± 0.02
15.0 – 20.0	1.20	+0.09 -0.09	+0.02 -0.04	± 0.25

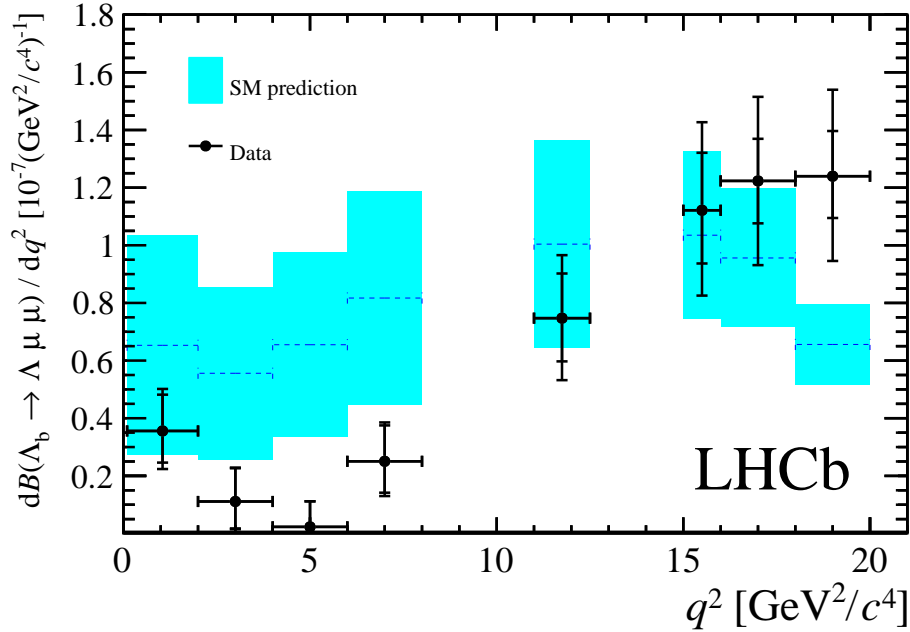


Figure 5: Measured $\Lambda_b^0 \rightarrow \Lambda \mu^+ \mu^-$ branching fraction as a function of q^2 with the predictions of the SM [15] superimposed. The inner error bars on data points represent the total uncertainty on the relative branching fraction (statistical and systematic); the outer error bar also includes the uncertainties from the branching fraction of the normalisation mode.

9 Angular analysis

The forward-backward asymmetries of both the dimuon system, A_{FB}^ℓ , and of the $p\pi$ system, A_{FB}^h , are defined as

$$A_{\text{FB}}^i(q^2) = \frac{\int_0^1 \frac{d^2\Gamma}{dq^2 d\cos\theta_i} d\cos\theta_i - \int_{-1}^0 \frac{d^2\Gamma}{dq^2 d\cos\theta_i} d\cos\theta_i}{d\Gamma/dq^2}, \quad (3)$$

where $d^2\Gamma/dq^2 d\cos\theta_i$ is the two-dimensional differential rate and $d\Gamma/dq^2$ is the rate integrated over the corresponding angles. The observables are determined by a fit to one-dimensional angular distributions as a function of $\cos\theta_\ell$, the angle between the positive (negative) muon direction and the dimuon system direction in the Λ_b^0 ($\bar{\Lambda}_b^0$) rest frame, and $\cos\theta_h$, which is defined as the angle between the proton and the Λ baryon directions, also in the Λ_b^0 rest frame. The differential rate as a function of $\cos\theta_\ell$ is described by the function

$$\frac{d^2\Gamma(\Lambda_b \rightarrow \Lambda \ell^+ \ell^-)}{dq^2 d\cos\theta_\ell} = \frac{d\Gamma}{dq^2} \left[\frac{3}{8} (1 + \cos^2\theta_\ell) (1 - f_L) + A_{\text{FB}}^\ell \cos\theta_\ell + \frac{3}{4} f_L \sin^2\theta_\ell \right], \quad (4)$$

where f_L is the fraction of longitudinally polarised dimuons. The rate as a function of $\cos\theta_h$ has the form

$$\frac{d^2\Gamma(\Lambda_b \rightarrow \Lambda(\rightarrow p\pi^-)\ell^+\ell^-)}{dq^2 d\cos\theta_h} = \mathcal{B}(\Lambda \rightarrow p\pi^-) \frac{d\Gamma(\Lambda_b \rightarrow \Lambda \ell^+ \ell^-)}{dq^2} \frac{1}{2} \left(1 + 2A_{\text{FB}}^h \cos\theta_h \right). \quad (5)$$

These expressions assume that Λ_b^0 baryons are produced unpolarised, which is in agreement with the measured production polarisation at LHCb [37].

The forward-backward asymmetries are measured in data using unbinned maximum likelihood fits. The signal PDF consists of a theoretical shape, given by Eqs. 4 and 5, multiplied by an acceptance function. Selection requirements on the minimum momentum of the muons may distort the $\cos\theta_\ell$ distribution by removing candidates with extreme values of $\cos\theta_\ell$. Similarly, the impact parameter requirements affect $\cos\theta_h$ as very forward hadrons tend to have smaller impact parameter values. The angular efficiency is parametrised using a second-order polynomial and determined separately for downstream and long candidates by fitting simulated events, with an independent set of parameters obtained for each q^2 interval. These parameters are fixed in the fits to data. The acceptances are shown in Fig. 6 as a function of $\cos\theta_h$ and $\cos\theta_\ell$ in the $15 < q^2 < 20$ GeV²/c⁴ interval for each candidate category.

The background shape is parametrised by the product of a linear function and the signal efficiency, with the value of the slope determined by fitting candidates in the upper mass sideband, $m(\Lambda\mu^+\mu^-) > 5700$ MeV/c². To limit systematic effects due to uncertainties in the background parametrisation, an invariant mass range that is dominated by signal events is used: $5580 < m(\Lambda\mu^+\mu^-) < 5660$ MeV/c². The ratio of signal to background events in this region is obtained by performing a fit to the invariant mass distribution in a wider mass interval.

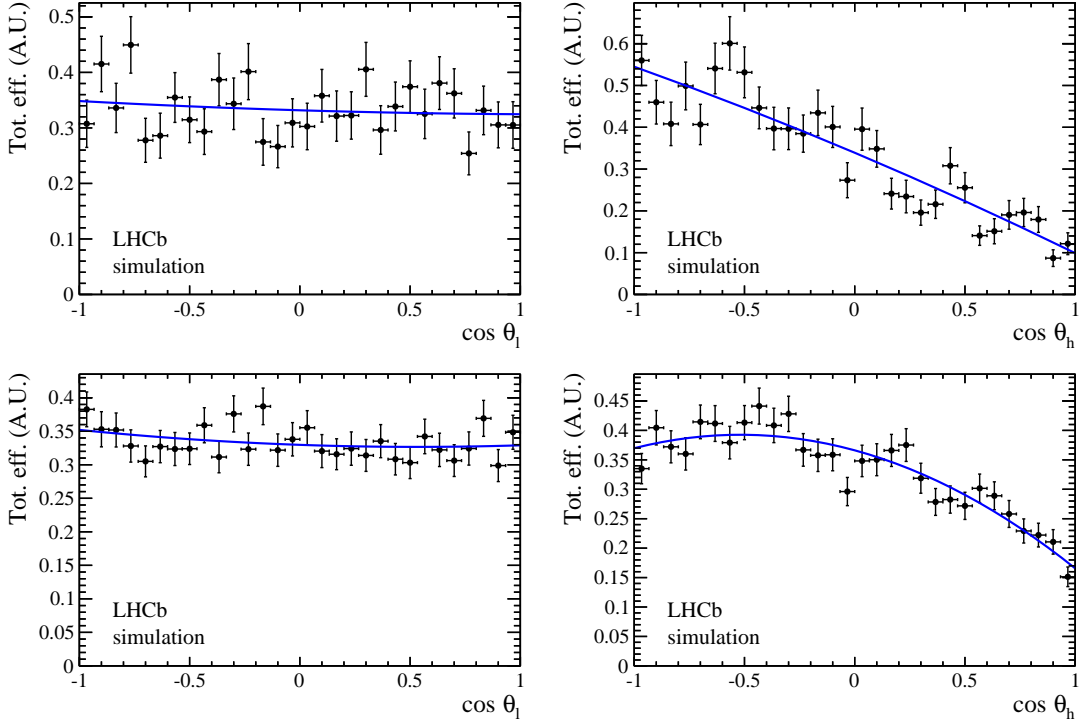


Figure 6: Angular efficiencies as a function of (left) $\cos\theta_\ell$ and (right) $\cos\theta_h$ for (upper) long and (lower) downstream candidates, in the interval $15 < q^2 < 20 \text{ GeV}^2/c^4$, obtained using simulated events. The (blue) line shows the fit that is used to model the angular acceptance in the fit to data.

The angular fit is performed simultaneously for the samples of downstream and long candidates, using separate acceptance and background functions for the two categories

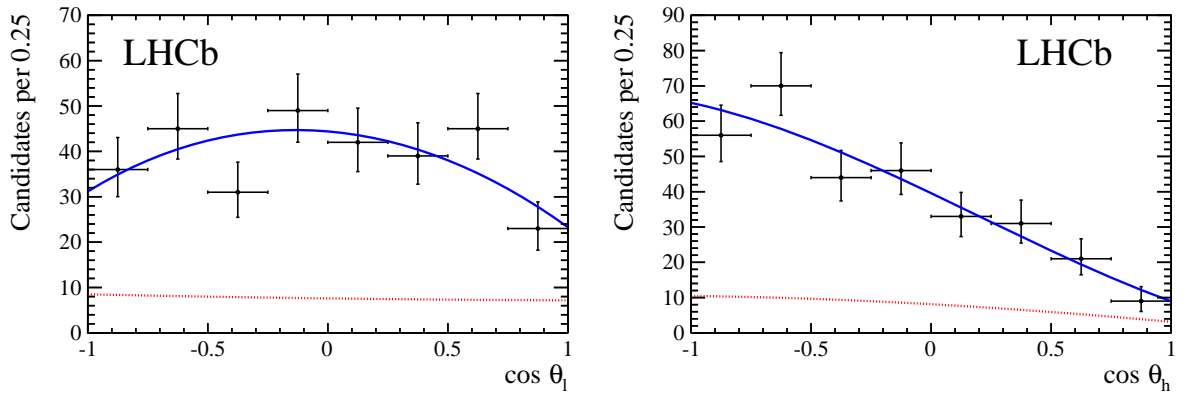


Figure 7: Angular distributions as a function of (left) $\cos\theta_\ell$ and (right) $\cos\theta_h$, for candidates in the integrated $15 < q^2 < 20 \text{ GeV}^2/c^4$ interval with the overall fit function overlaid (solid blue). The (red) dotted line represents the combinatorial background.

while keeping the angular observables as shared parameters. Angular distributions are shown in Fig. 7 where the two candidate categories are combined.

10 Systematic uncertainties on angular observables

10.1 Angular correlations

To derive Eqs. 4 and 5, a uniform efficiency is assumed. However, non-uniformity is observed, especially as a function of $\cos\theta_h$ (see Fig. 6). Therefore, while integrating over the full angular distribution, terms that would cancel with constant efficiency may remain and generate a bias in the measurement of these observables. To assess the impact of this potential bias, simulated experiments are generated in a two-dimensional $(\cos\theta_\ell, \cos\theta_h)$ space according to the theoretical distribution multiplied by a two-dimensional efficiency histogram. Projections are then made and are fitted with the default one-dimensional efficiency functions. The average deviations from the generated parameters are assigned as systematic uncertainties. The magnitudes of these are found to be -0.032 for A_{FB}^ℓ , 0.013 for A_{FB}^h and 0.028 for f_L , independently of q^2 . In most q^2 intervals this is the dominant source of systematic uncertainty.

10.2 Resolution

Resolution effects may induce an asymmetric migration of events between bins and therefore generate a bias in the measured value of the forward-backward asymmetries. To study this systematic effect, a map of the angular resolution function is created using simulated events by comparing reconstructed quantities with those in the absence of resolution effects. Simulated experiments are then generated according to the measured angular distributions and smeared using the angular resolution maps. The simulated events, before and after smearing by the angular resolution function, are fitted with the default PDF. The average deviations from the default values are assigned as systematic uncertainties. These are larger for the A_{FB}^h observable because the resolution is poorer for $\cos\theta_h$ and the distribution is more asymmetric, yielding a net migration effect. The uncertainties from this source are in the ranges $[0.011, 0.016]$ for A_{FB}^ℓ , $[-0.001, -0.007]$ for A_{FB}^h and $[0.002, 0.008]$ for f_L , depending on q^2 .

10.3 Angular acceptance

An imprecise determination of the efficiency due to data-simulation discrepancies could bias the A_{FB} measurement. To estimate the potential impact arising from this source, the kinematic reweighting described in Sec. 7.2 is removed from the simulation. Simulated samples are fitted using the same theoretical PDF multiplied by the efficiency function obtained with and without kinematical reweighting. The average biases evaluated from simulated experiments are assigned as systematic uncertainties. These are larger for sparsely

Table 5: Measured values of leptonic and hadronic angular observables, where the first uncertainties are statistical and the second systematic.

q^2 interval [GeV ² /c ⁴]	A_{FB}^ℓ	f_L	A_{FB}^h
0.1 – 2.0	$0.37^{+0.37}_{-0.48} \pm 0.03$	$0.56^{+0.23}_{-0.56} \pm 0.08$	$-0.12^{+0.31}_{-0.28} \pm 0.15$
11.0 – 12.5	$0.01^{+0.19}_{-0.18} \pm 0.06$	$0.40^{+0.37}_{-0.36} \pm 0.06$	$-0.50^{+0.10}_{-0.00} \pm 0.04$
15.0 – 16.0	$-0.10^{+0.18}_{-0.16} \pm 0.03$	$0.49^{+0.30}_{-0.30} \pm 0.05$	$-0.19^{+0.14}_{-0.16} \pm 0.03$
16.0 – 18.0	$-0.07^{+0.13}_{-0.12} \pm 0.04$	$0.68^{+0.15}_{-0.21} \pm 0.05$	$-0.44^{+0.10}_{-0.05} \pm 0.03$
18.0 – 20.0	$0.01^{+0.15}_{-0.14} \pm 0.04$	$0.62^{+0.24}_{-0.27} \pm 0.04$	$-0.13^{+0.09}_{-0.12} \pm 0.03$
15.0 – 20.0	$-0.05^{+0.09}_{-0.09} \pm 0.03$	$0.61^{+0.11}_{-0.14} \pm 0.03$	$-0.29^{+0.07}_{-0.07} \pm 0.03$

populated q^2 intervals and vary in the intervals [0.009, 0.016] for A_{FB}^ℓ , [0.001, 0.007] for A_{FB}^h and [0.002, 0.044] for f_L , depending on q^2 .

The effect of the limited knowledge of the A_b^0 polarisation is investigated by varying the polarisation within its measured uncertainties, in the same way as for the branching fraction measurement. No significant effect is found and therefore no contribution is assigned.

10.4 Background parametrisation

As there is ambiguity in the choice of parametrisation for the background model, in particular for regions with low statistical significance in data, simulated experiments are generated from a PDF corresponding to the best fit to data, for each q^2 interval. Each simulated sample is fitted with two models: the nominal fit model, consisting of the product of a linear function and the signal efficiency, and an alternative model formed from a constant function multiplied by the efficiency shape. The average deviations are taken as systematic uncertainties. These are in the ranges [0.003, 0.045] for A_{FB}^ℓ , [0.017, 0.053] for A_{FB}^h and [0.014, 0.049] for f_L , depending on q^2 .

11 Results of the angular analysis

The angular analysis is performed using the same q^2 intervals as those used in the branching fraction measurement. Results are reported for each q^2 interval in which the statistical significance of the signal is at least three standard deviations. This includes all of the q^2 intervals above the J/ψ resonance and the lowest q^2 bin.

The measured values of the leptonic and hadronic forward-backward asymmetries, A_{FB}^ℓ ² and A_{FB}^h , and the f_L observable are summarised in Table 5, with the asymmetries shown in Fig. 8. The statistical uncertainties are obtained using the likelihood-ratio ordering

²During preparation of update mistake in the analysis was identified, which changes the meaning of the measured quantity. Please see appendix B for details.

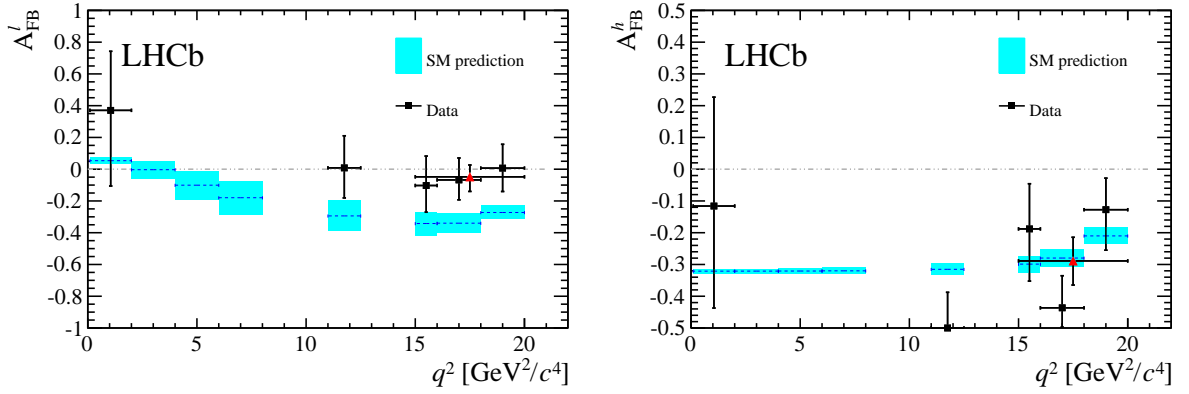


Figure 8: Measured values of (left) the leptonic and (right) the hadronic forward-backward asymmetries in bins of q^2 . Data points are only shown for q^2 intervals where a statistically significant signal yield is found, see text for details. The (red) triangle represents the values for the $15 < q^2 < 20$ GeV^2/c^4 interval. Standard Model predictions are obtained from Ref. [17].

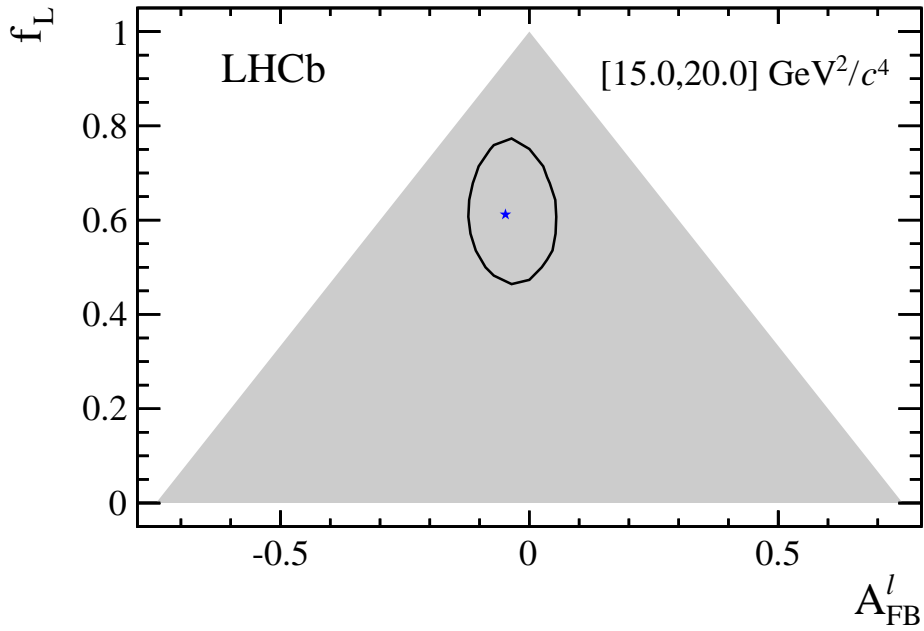


Figure 9: Two-dimensional 68% CL region (black) as a function of A_{FB}^l and f_L . The shaded area represents the region where the PDF is positive over the complete $\cos \theta_\ell$ range. The best fit point is given by the (blue) star.

method [48] where only one of the two observables at a time is treated as the parameter of interest. In this analysis nuisance parameters were accounted for using the plug-in method [49]. In Fig. 9 the statistical uncertainties on A_{FB}^l and f_L are also reported (for the interval $15 < q^2 < 20$ GeV^2/c^4) as a two-dimensional 68% confidence level (CL) region,

where the likelihood-ratio ordering method is applied by varying both observables and therefore taking correlations into account. Confidence regions for the other q^2 intervals are shown in Fig. 10, see Appendix.

12 Conclusions

A measurement of the differential branching fraction of the $\Lambda_b^0 \rightarrow \Lambda \mu^+ \mu^-$ decay is performed using data, corresponding to an integrated luminosity of 3.0 fb^{-1} , recorded by the LHCb detector at centre-of-mass energies of 7 and 8 TeV. Signal is observed for the first time at a significance of more than three standard deviations in two q^2 intervals: $0.1 < q^2 < 2.0 \text{ GeV}^2/c^4$, close to the photon pole, and between the charmonium resonances. No significant signal is observed in the $1.1 < q^2 < 6.0 \text{ GeV}^2/c^4$ range. The uncertainties of the measurements in the region $15 < q^2 < 20 \text{ GeV}^2/c^4$ are reduced by a factor of approximately three relative to previous LHCb measurements [19]. The improvements in the results, which supersede those of Ref. [19], are due to the larger data sample size and a better control of systematic uncertainties. The measurements are compatible with the predictions of the Standard Model in the high- q^2 region and lie below the predictions in the low- q^2 region.

The first measurement of angular observables for the $\Lambda_b^0 \rightarrow \Lambda \mu^+ \mu^-$ decay is reported, in the form of two forward-backward asymmetries, in the dimuon and $p\pi$ systems and the fraction of longitudinally polarised dimuons. The measurements of the A_{FB}^h observable are in good agreement with the predictions of the SM, while for the A_{FB}^ℓ observable measurements are consistently above the prediction.

A Appendix

The measured values of the branching fraction of the $\Lambda_b^0 \rightarrow \Lambda \mu^+ \mu^-$ decay normalised to $\Lambda_b^0 \rightarrow J/\psi \Lambda$ decays are given in Table 6, where the statistical and total systematic uncertainties are shown separately.

Table 6: Differential branching fraction of the $\Lambda_b^0 \rightarrow \Lambda \mu^+ \mu^-$ decay relative to $\Lambda_b^0 \rightarrow J/\psi \Lambda$ decays, where the uncertainties are statistical and systematic, respectively.

q^2 interval [GeV^2/c^4]	$\frac{d\mathcal{B}(\Lambda_b^0 \rightarrow \Lambda \mu^+ \mu^-)/dq^2}{\mathcal{B}(\Lambda_b^0 \rightarrow J/\psi \Lambda)} \cdot 10^{-3} [(\text{GeV}^2/c^4)^{-1}]$		
0.1 – 2.0	0.56	+0.20 –0.17	+0.03 –0.03
2.0 – 4.0	0.18	+0.18 –0.15	+0.01 –0.01
4.0 – 6.0	0.04	+0.14 –0.04	+0.01 –0.01
6.0 – 8.0	0.40	+0.20 –0.17	+0.01 –0.02
11.0 – 12.5	1.19	+0.24 –0.23	+0.04 –0.07
15.0 – 16.0	1.78	+0.31 –0.28	+0.08 –0.08
16.0 – 18.0	1.94	+0.23 –0.22	+0.04 –0.09
18.0 – 20.0	1.97	+0.23 –0.22	+0.10 –0.07
1.1–6.0	0.14	+0.10 –0.09	+0.01 –0.01
15.0–20.0	1.90	+0.14 –0.14	+0.04 –0.06

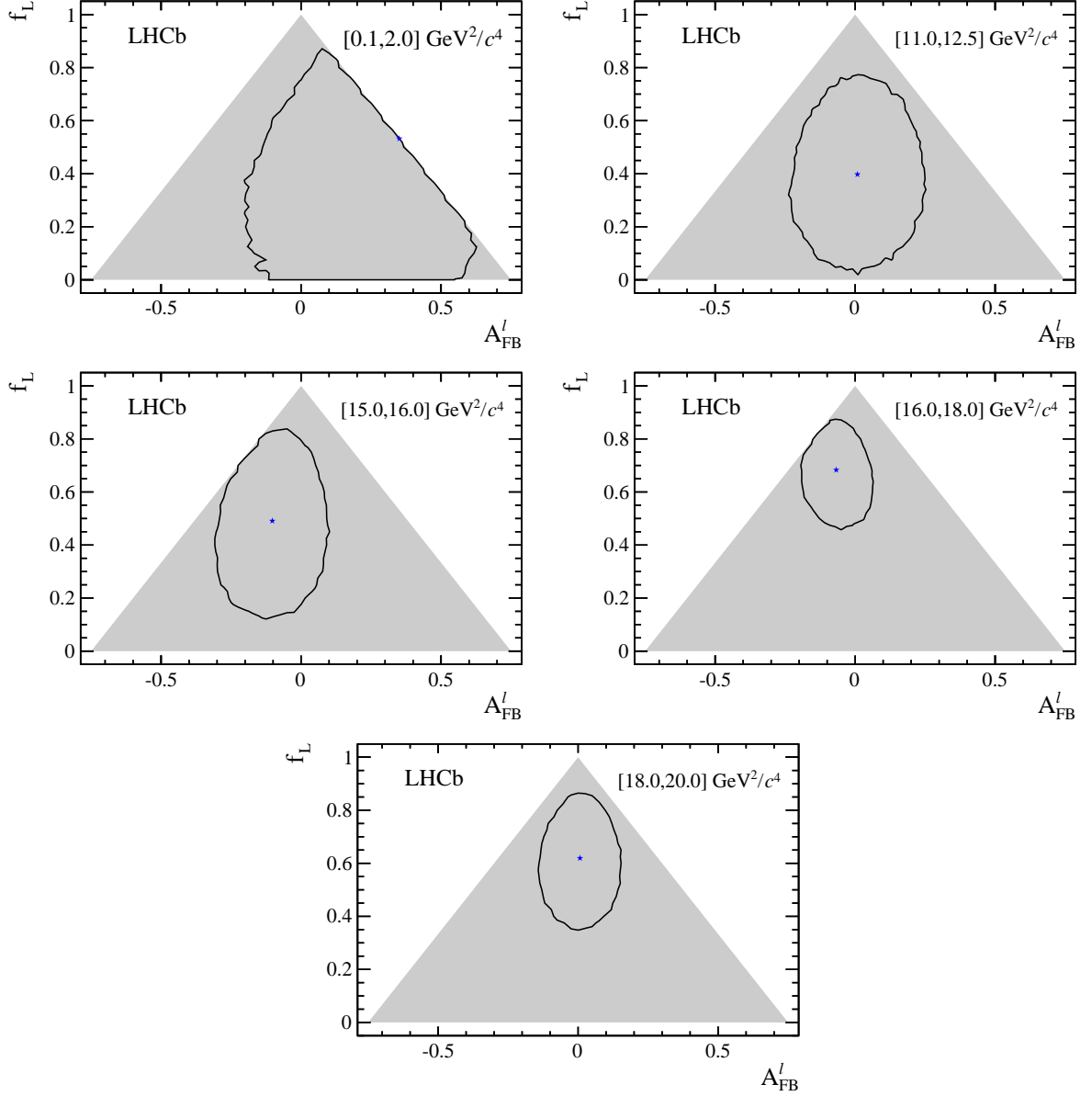


Figure 10: Two-dimensional 68% CL regions (black) as a function of A_{FB}^l and f_L . The shaded areas represent the regions in which the PDF is positive over the complete $\cos\theta_\ell$ range. The best fit points are indicated by the (blue) stars.

The two-dimensional 68% CL regions for the observables A_{FB}^l and f_L are given in Fig 10, for each q^2 interval in which signal is observed.

B Erratum

The angular distribution of the dimuon system of the decays $\Lambda_b^0 \rightarrow \Lambda \mu^+ \mu^-$ and $\bar{\Lambda}_b^0 \rightarrow \bar{\Lambda} \mu^+ \mu^-$ can be described by

$$\frac{d\Gamma}{d \cos \theta_\ell} = \frac{3}{8}(1 + \cos^2 \theta_\ell)(1 - f_L) + A_{\text{FB}}^\ell \cos \theta_\ell + \frac{3}{4}f_L \sin^2 \theta_\ell , \quad (6)$$

where A_{FB}^ℓ is the forward-backward asymmetry of the dimuon system and f_L is its longitudinal polarisation fraction. For the Λ_b^0 decay, the angle θ_ℓ is calculated as the angle between the direction of the μ^+ lepton, in the rest frame of the dimuon pair, and the direction of the dimuon pair, in the rest frame of the Λ_b^0 decay. The forward-backward asymmetry of the lepton pair, A_{FB}^ℓ , is “odd” under CP conjugation and changes in sign between the Λ_b^0 and $\bar{\Lambda}_b^0$ decays. To compensate for this sign, the angle θ_ℓ is usually calculated from the μ^- lepton rather than the μ^+ lepton such that A_{FB}^ℓ can be calculated from the combined sample. This was the intended approach of this paper. Unfortunately, A_{FB}^ℓ was determined using the μ^+ lepton when determining θ_ℓ for both the Λ_b^0 and the $\bar{\Lambda}_b^0$ decays. Consequently, the value of A_{FB}^ℓ in this paper corresponds to a difference $A(A_{\text{FB}}^\ell)$ in asymmetries between the Λ_b^0 and $\bar{\Lambda}_b^0$ decays rather than a proper average and is expected to be zero if CP is conserved. The result quoted as A_{FB}^ℓ in this paper should therefore be interpreted as

$$A(A_{\text{FB}}^\ell) = -0.05 \pm 0.09 \text{ (stat)} \pm 0.03 \text{ (syst)} , \quad (7)$$

and is indeed consistent with the Standard Model expectation that CP violating effects should be small in the decay $\Lambda_b^0 \rightarrow \Lambda \mu^+ \mu^-$. This is in itself a useful result. A measurement of A_{FB}^ℓ has since been presented in Ref. [50]. The results in Ref. [50] supersede the corresponding results in this paper. Note, the mistake in the angular definition only affects the value of A_{FB}^ℓ presented in the paper. The values of A_{FB}^h and the differential branching fraction are unchanged, due to the symmetry of the efficiency model in $\cos \theta_\ell$.

Acknowledgements

We express our gratitude to our colleagues in the CERN accelerator departments for the excellent performance of the LHC. We thank the technical and administrative staff at the LHCb institutes. We acknowledge support from CERN and from the national agencies: CAPES, CNPq, FAPERJ and FINEP (Brazil); NSFC (China); CNRS/IN2P3 (France); BMBF, DFG, HGF and MPG (Germany); INFN (Italy); FOM and NWO (The Netherlands); MNiSW and NCN (Poland); MEN/IFA (Romania); MinES and FANO (Russia); MinCo (Spain); SNSF and SER (Switzerland); NASU (Ukraine); STFC (United Kingdom); NSF (USA). The Tier1 computing centres are supported by IN2P3 (France), KIT and BMBF (Germany), INFN (Italy), NWO and SURF (The Netherlands), PIC (Spain), GridPP (United Kingdom). We are indebted to the communities behind the multiple open source software packages on which we depend. We are also thankful for the computing resources and the access to software R&D tools provided by Yandex LLC (Russia). Individual groups or members have received support from EPLANET, Marie Skłodowska-Curie Actions and ERC (European Union), Conseil général de Haute-Savoie, Labex ENIGMASS and OCEVU, Région Auvergne (France), RFBR (Russia), XuntaGal and GENCAT (Spain), Royal Society and Royal Commission for the Exhibition of 1851 (United Kingdom).

References

- [1] T. Mannel and S. Recksiegel, *Flavour-changing neutral current decays of heavy baryons. The case $\Lambda_b^0 \rightarrow \Lambda \gamma$* , J. Phys. **G24** (1998) 979, [arXiv:hep-ph/9701399](#).
- [2] G. Hiller, M. Knecht, F. Legger, and T. Schietinger, *Photon polarization from helicity suppression in radiative decays of polarized Λ_b^0 to spin-3/2 baryons*, Phys. Lett. **B649** (2007) 152, [arXiv:hep-ph/0702191](#).
- [3] P. Ber, T. Feldmann, and D. van Dyk, *Angular analysis of the decay $\Lambda_b \rightarrow \Lambda(\rightarrow N\pi)\ell^+\ell^-$* , JHEP **01** (2015) 155, [arXiv:1410.2115](#).
- [4] M. J. Aslam, Y.-M. Wang, and C.-D. Lu, *Exclusive semileptonic decays of $\Lambda_b^0 \rightarrow \Lambda \ell^+\ell^-$ in supersymmetric theories*, Phys. Rev. **D78** (2008) 114032, [arXiv:0808.2113](#).
- [5] Y.-M. Wang, Y. Li, and C.-D. Lu, *Rare decays of $\Lambda_b^0 \rightarrow \Lambda + \gamma$ and $\Lambda_b^0 \rightarrow \Lambda + \ell^+\ell^-$ in the light-cone sum rules*, Eur. Phys. J. **C59** (2009) 861, [arXiv:0804.0648](#).
- [6] C.-S. Huang and H.-G. Yan, *Exclusive rare decays of heavy baryons to light baryons: $\Lambda_b^0 \rightarrow \Lambda \gamma$ and $\Lambda_b^0 \rightarrow \Lambda \ell^+\ell^-$* , Phys. Rev. **D59** (1999) 114022, [arXiv:hep-ph/9811303](#).
- [7] C.-H. Chen and C. Q. Geng, *Rare $\Lambda_b^0 \rightarrow \Lambda \ell^+\ell^-$ decays with polarized Λ* , Phys. Rev. **D63** (2001) 114024, [arXiv:hep-ph/0101171](#).

- [8] C.-H. Chen and C. Q. Geng, *Baryonic rare decays of $\Lambda_b^0 \rightarrow \Lambda \ell^+ \ell^-$* , Phys. Rev. **D64** (2001) 074001, [arXiv:hep-ph/0106193](#).
- [9] C.-H. Chen and C. Q. Geng, *Lepton asymmetries in heavy baryon decays of $\Lambda_b^0 \rightarrow \Lambda \ell^+ \ell^-$* , Phys. Lett. **B516** (2001) 327, [arXiv:hep-ph/0101201](#).
- [10] F. Zolfagharpour and V. Bashiry, *Double lepton polarization in $\Lambda_b^0 \rightarrow \Lambda \ell^+ \ell^-$ decay in the Standard Model with fourth generations scenario*, Nucl. Phys. **B796** (2008) 294, [arXiv:0707.4337](#).
- [11] L. Mott and W. Roberts, *Rare dileptonic decays of Λ_b^0 in a quark model*, Int. J. Mod. Phys. **A27** (2012) 1250016, [arXiv:1108.6129](#).
- [12] T. M. Aliev, K. Azizi, and M. Savci, *Analysis of the $\Lambda_b^0 \rightarrow \Lambda \ell^+ \ell^-$ decay in QCD*, Phys. Rev. **D81** (2010) 056006, [arXiv:1001.0227](#).
- [13] R. Mohanta and A. K. Giri, *Fourth generation effect on Λ_b^0 decays*, Phys. Rev. **D82** (2010) 094022, [arXiv:1010.1152](#).
- [14] S. Sahoo, C. K. Das, and L. Maharana, *Effect of both Z and Z' -mediated flavor-changing neutral currents on the baryonic rare decay $\Lambda_b^0 \rightarrow \Lambda \ell^+ \ell^-$* , Int. J. Mod. Phys. **A24** (2009) 6223, [arXiv:1112.4563](#).
- [15] W. Detmold, C.-J. D. Lin, S. Meinel, and M. Wingate, *$\Lambda_b^0 \rightarrow \Lambda \ell^+ \ell^-$ form factors and differential branching fraction from lattice QCD*, Phys. Rev. **D87** (2013) 074502, [arXiv:1212.4827](#).
- [16] T. Gutsche *et al.*, *Rare baryon decays $\Lambda_b^0 \rightarrow \Lambda \ell^+ \ell^-$ ($\ell = e, \mu, \tau$) and $\Lambda_b^0 \rightarrow \Lambda \gamma$: differential and total rates, lepton- and hadron-side forward-backward asymmetries*, Phys. Rev. **D87** (2013) 074031, [arXiv:1301.3737](#).
- [17] S. Meinel, *Flavor physics with Λ_b baryons*, PoS **LATTICE2013** (2014) 024, [arXiv:1401.2685](#).
- [18] CDF collaboration, T. Aaltonen *et al.*, *Observation of the baryonic flavor-changing neutral current decay $\Lambda_b^0 \rightarrow \Lambda \mu^+ \mu^-$* , Phys. Rev. Lett. **107** (2011) 201802, [arXiv:1107.3753](#).
- [19] LHCb collaboration, R. Aaij *et al.*, *Measurement of the differential branching fraction of the decay $\Lambda_b^0 \rightarrow \Lambda \mu^+ \mu^-$* , Phys. Lett. **B725** (2013) 25, [arXiv:1306.2577](#).
- [20] M. Beylich, G. Buchalla, and T. Feldmann, *Theory of $B \rightarrow K^{(*)} \ell^+ \ell^-$ decays at high q^2 : OPE and quark-hadron duality*, Eur. Phys. J. **C71** (2011) 1635, [arXiv:1101.5118](#).
- [21] M. Beneke and T. Feldmann, *Symmetry breaking corrections to heavy to light B meson form-factors at large recoil*, Nucl. Phys. **B592** (2001) 3, [arXiv:hep-ph/0008255](#).

- [22] LHCb collaboration, A. A. Alves Jr. *et al.*, *The LHCb detector at the LHC*, JINST **3** (2008) S08005.
- [23] LHCb collaboration, R. Aaij *et al.*, *LHCb detector performance*, Int. J. Mod. Phys. **A30** (2015) 1530022, arXiv:1412.6352.
- [24] R. Aaij *et al.*, *Performance of the LHCb Vertex Locator*, JINST **9** (2014) P09007, arXiv:1405.7808.
- [25] R. Arink *et al.*, *Performance of the LHCb Outer Tracker*, JINST **9** (2014) P01002, arXiv:1311.3893.
- [26] M. Adinolfi *et al.*, *Performance of the LHCb RICH detector at the LHC*, Eur. Phys. J. **C73** (2013) 2431, arXiv:1211.6759.
- [27] A. A. Alves Jr. *et al.*, *Performance of the LHCb muon system*, JINST **8** (2013) P02022, arXiv:1211.1346.
- [28] R. Aaij *et al.*, *The LHCb trigger and its performance in 2011*, JINST **8** (2013) P04022, arXiv:1211.3055.
- [29] T. Sjöstrand, S. Mrenna, and P. Skands, *A brief introduction to PYTHIA 8.1*, Comput. Phys. Commun. **178** (2008) 852, arXiv:0710.3820.
- [30] I. Belyaev *et al.*, *Handling of the generation of primary events in GAUSS, the LHCb simulation framework*, Nuclear Science Symposium Conference Record (NSS/MIC) **IEEE** (2010) 1155.
- [31] D. J. Lange, *The EvtGen particle decay simulation package*, Nucl. Instrum. Meth. **A462** (2001) 152.
- [32] P. Golonka and Z. Was, *PHOTOS Monte Carlo: A precision tool for QED corrections in Z and W decays*, Eur. Phys. J. **C45** (2006) 97, arXiv:hep-ph/0506026.
- [33] GEANT4 collaboration, J. Allison *et al.*, *Geant4 developments and applications*, IEEE Trans. Nucl. Sci. **53** (2006) 270; GEANT4 collaboration, S. Agostinelli *et al.*, *GEANT4: A simulation toolkit*, Nucl. Instrum. Meth. **A506** (2003) 250.
- [34] M. Clemencic *et al.*, *The LHCb simulation application, GAUSS: Design, evolution and experience*, J. of Phys. : Conf. Ser. **331** (2011) 032023.
- [35] A. J. Buras and M. Munz, *Effective hamiltonian for $B \rightarrow X_s e^+ e^-$ beyond leading logarithms in the naïve dimensional regularization and 't Hooft-Veltman schemes*, Phys. Rev. **D52** (1995) 186, arXiv:hep-ph/9501281.
- [36] A. J. Buras, M. Misiak, M. Munz, and S. Pokorski, *Theoretical uncertainties and phenomenological aspects of $B \rightarrow X_s \gamma$ decay*, Nucl. Phys. **B424** (1994) 374, arXiv:hep-ph/9311345.

- [37] LHCb collaboration, R. Aaij *et al.*, *Measurements of the $\Lambda_b^0 \rightarrow J/\psi \Lambda$ decay amplitudes and the Λ_b^0 polarisation in pp collisions at $\sqrt{s} = 7$ TeV*, Phys. Lett. **B724** (2013) 27, arXiv:1302.5578.
- [38] Particle Data Group, K. A. Olive *et al.*, *Review of particle physics*, Chin. Phys. **C38** (2014) 090001.
- [39] W. D. Hulsbergen, *Decay chain fitting with a Kalman filter*, Nucl. Instrum. Meth. **A552** (2005) 566, arXiv:physics/0503191.
- [40] M. Feindt and U. Kerzel, *The NeuroBayes neural network package*, Nucl. Instrum. Meth. **A559** (2006) 190.
- [41] M. Feindt, *A neural Bayesian estimator for conditional probability densities*, arXiv:physics/0402093.
- [42] G. Punzi, *Sensitivity of searches for new signals and its optimization*, eConf **C030908** (2003) MODT002, arXiv:physics/0308063.
- [43] T. Skwarnicki, *A study of the radiative cascade transitions between the Upsilon-prime and Upsilon resonances*, PhD thesis, Institute of Nuclear Physics, Krakow, 1986, DESY-F31-86-02.
- [44] T. M. Aliev and M. Savci, *Polarization effects in exclusive semileptonic $\Lambda_b^0 \rightarrow \Lambda \ell^+ \ell^-$ decay*, JHEP **05** (2006) 001, arXiv:hep-ph/0507324.
- [45] S. Descotes-Genon, J. Matias, and J. Virto, *Understanding the $B \rightarrow K^* \mu^+ \mu^-$ anomaly*, Phys. Rev. **D88** (2013), no. 7 074002, arXiv:1307.5683.
- [46] LHCb collaboration, R. Aaij *et al.*, *Differential branching fractions and isospin asymmetries of $B \rightarrow K^* \mu^+ \mu^-$ decays*, JHEP **06** (2014) 133, arXiv:1403.8044.
- [47] LHCb collaboration, R. Aaij *et al.*, *Precision measurement of the ratio of the Λ_b^0 to \bar{B}^0 lifetimes*, Phys. Lett. **B734** (2014) 122, arXiv:1402.6242.
- [48] G. J. Feldman and R. D. Cousins, *Unified approach to the classical statistical analysis of small signals*, Phys. Rev. **D57** (1998) 3873, arXiv:physics/9711021.
- [49] B. Sen, M. Walker, and M. Woodroffe, *On the unified method with nuisance parameters*, Statistica Sinica **19** (2009) 301.
- [50] LHCb collaboration, R. Aaij *et al.*, *Angular moments of the decay $\Lambda_b^0 \rightarrow \Lambda \mu^+ \mu^-$* , JHEP **09** (2018) 146, arXiv:1808.00264.

LHCb collaboration

R. Aaij⁴¹, B. Adeva³⁷, M. Adinolfi⁴⁶, A. Affolder⁵², Z. Ajaltouni⁵, S. Akar⁶, J. Albrecht⁹, F. Alessio³⁸, M. Alexander⁵¹, S. Ali⁴¹, G. Alkhazov³⁰, P. Alvarez Cartelle⁵³, A.A. Alves Jr⁵⁷, S. Amato², S. Amerio²², Y. Amhis⁷, L. An³, L. Anderlini^{17,g}, J. Anderson⁴⁰, M. Andreotti^{16,f}, J.E. Andrews⁵⁸, R.B. Appleby⁵⁴, O. Aquines Gutierrez¹⁰, F. Archilli³⁸, A. Artamonov³⁵, M. Artuso⁵⁹, E. Aslanides⁶, G. Auriemma^{25,n}, M. Baalouch⁵, S. Bachmann¹¹, J.J. Back⁴⁸, A. Badalov³⁶, C. Baesso⁶⁰, W. Baldini^{16,38}, R.J. Barlow⁵⁴, C. Barschel³⁸, S. Barsuk⁷, W. Barter³⁸, V. Batozskaya²⁸, V. Battista³⁹, A. Bay³⁹, L. Beaucourt⁴, J. Beddow⁵¹, F. Bedeschi²³, I. Bediaga¹, L.J. Bel⁴¹, I. Belyaev³¹, E. Ben-Haim⁸, G. Bencivenni¹⁸, S. Benson³⁸, J. Benton⁴⁶, A. Berezhnoy³², R. Bernet⁴⁰, A. Bertolin²², M.-O. Bettler³⁸, M. van Beuzekom⁴¹, A. Bien¹¹, S. Bifani⁴⁵, T. Bird⁵⁴, A. Bizzeti^{17,i}, T. Blake⁴⁸, F. Blanc³⁹, J. Blouw¹⁰, S. Blusk⁵⁹, V. Bocci²⁵, A. Bondar³⁴, N. Bondar^{30,38}, W. Bonivento¹⁵, S. Borghi⁵⁴, M. Borsato⁷, T.J.V. Bowcock⁵², E. Bowen⁴⁰, C. Bozzi¹⁶, S. Braun¹¹, D. Brett⁵⁴, M. Britsch¹⁰, T. Britton⁵⁹, J. Brodzicka⁵⁴, N.H. Brook⁴⁶, A. Bursche⁴⁰, J. Buytaert³⁸, S. Cadeddu¹⁵, R. Calabrese^{16,f}, M. Calvi^{20,k}, M. Calvo Gomez^{36,p}, P. Campana¹⁸, D. Campora Perez³⁸, L. Capriotti⁵⁴, A. Carbone^{14,d}, G. Carboni^{24,l}, R. Cardinale^{19,j}, A. Cardini¹⁵, P. Carniti²⁰, L. Carson⁵⁰, K. Carvalho Akiba^{2,38}, R. Casanova Mohr³⁶, G. Casse⁵², L. Cassina^{20,k}, L. Castillo Garcia³⁸, M. Cattaneo³⁸, Ch. Cauet⁹, G. Cavallero¹⁹, R. Cenci^{23,t}, M. Charles⁸, Ph. Charpentier³⁸, M. Chefdeville⁴, S. Chen⁵⁴, S.-F. Cheung⁵⁵, N. Chiapolini⁴⁰, M. Chrzaszcz^{40,26}, X. Cid Vidal³⁸, G. Ciezarek⁴¹, P.E.L. Clarke⁵⁰, M. Clemencic³⁸, H.V. Cliff⁴⁷, J. Closier³⁸, V. Coco³⁸, J. Cogan⁶, E. Cogneras⁵, V. Cogoni^{15,e}, L. Cojocariu²⁹, G. Collazuol²², P. Collins³⁸, A. Comerma-Montells¹¹, A. Contu^{15,38}, A. Cook⁴⁶, M. Coombes⁴⁶, S. Coquereau⁸, G. Corti³⁸, M. Corvo^{16,f}, I. Counts⁵⁶, B. Couturier³⁸, G.A. Cowan⁵⁰, D.C. Craik⁴⁸, A.C. Crocombe⁴⁸, M. Cruz Torres⁶⁰, S. Cunliffe⁵³, R. Currie⁵³, C. D'Ambrosio³⁸, J. Dalseno⁴⁶, P.N.Y. David⁴¹, A. Davis⁵⁷, K. De Bruyn⁴¹, S. De Capua⁵⁴, M. De Cian¹¹, J.M. De Miranda¹, L. De Paula², W. De Silva⁵⁷, P. De Simone¹⁸, C.-T. Dean⁵¹, D. Decamp⁴, M. Deckenhoff⁹, L. Del Buono⁸, N. Déléage⁴, D. Derkach⁵⁵, O. Deschamps⁵, F. Dettori³⁸, B. Dey⁴⁰, A. Di Canto³⁸, F. Di Ruscio²⁴, H. Dijkstra³⁸, S. Donleavy⁵², F. Dordei¹¹, M. Dorigo³⁹, A. Dosil Suárez³⁷, D. Dossett⁴⁸, A. Dovbnya⁴³, K. Dreimanis⁵², G. Dujany⁵⁴, F. Dupertuis³⁹, P. Durante³⁸, R. Dzhelyadin³⁵, A. Dziurda²⁶, A. Dzyuba³⁰, S. Easo^{49,38}, U. Egede⁵³, V. Egorychev³¹, S. Eidelman³⁴, S. Eisenhardt⁵⁰, U. Eitschberger⁹, R. Ekelhof⁹, L. Eklund⁵¹, I. El Rifai⁵, Ch. Elsasser⁴⁰, S. Ely⁵⁹, S. Esen¹¹, H.M. Evans⁴⁷, T. Evans⁵⁵, A. Falabella¹⁴, C. Färber¹¹, C. Farinelli⁴¹, N. Farley⁴⁵, S. Farry⁵², R. Fay⁵², D. Ferguson⁵⁰, V. Fernandez Albor³⁷, F. Ferrari¹⁴, F. Ferreira Rodrigues¹, M. Ferro-Luzzi³⁸, S. Filippov³³, M. Fiore^{16,38,f}, M. Fiorini^{16,f}, M. Firlej²⁷, C. Fitzpatrick³⁹, T. Fiutowski²⁷, P. Fol⁵³, M. Fontana¹⁰, F. Fontanelli^{19,j}, R. Forty³⁸, O. Francisco², M. Frank³⁸, C. Frei³⁸, M. Frosini¹⁷, J. Fu^{21,38}, E. Furfaro^{24,l}, A. Gallas Torreira³⁷, D. Galli^{14,d}, S. Gallorini^{22,38}, S. Gambetta^{19,j}, M. Gandelman², P. Gandini⁵⁵, Y. Gao³, J. García Pardiñas³⁷, J. Garofoli⁵⁹, J. Garra Tico⁴⁷, L. Garrido³⁶, D. Gascon³⁶, C. Gaspar³⁸, U. Gastaldi¹⁶, R. Gauld⁵⁵, L. Gavardi⁹, G. Gazzoni⁵, A. Geraci^{21,v}, D. Gerick¹¹, E. Gersabeck¹¹, M. Gersabeck⁵⁴, T. Gershon⁴⁸, Ph. Ghez⁴, A. Gianelle²², S. Giani³⁹, V. Gibson⁴⁷, L. Giubega²⁹, V.V. Gligorov³⁸, C. Göbel⁶⁰, D. Golubkov³¹, A. Golutvin^{53,31,38}, A. Gomes^{1,a}, C. Gotti^{20,k}, M. Grabalosa Gándara⁵, R. Graciani Diaz³⁶, L.A. Granado Cardoso³⁸, E. Graugés³⁶, E. Graverini⁴⁰, G. Graziani¹⁷, A. Grecu²⁹, E. Greening⁵⁵, S. Gregson⁴⁷, P. Griffith⁴⁵, L. Grillo¹¹, O. Grünberg⁶³, B. Gui⁵⁹, E. Gushchin³³, Yu. Guz^{35,38}, T. Gys³⁸, C. Hadjivasiliou⁵⁹, G. Haefeli³⁹, C. Haen³⁸,

S.C. Haines⁴⁷, S. Hall⁵³, B. Hamilton⁵⁸, T. Hampson⁴⁶, X. Han¹¹, S. Hansmann-Menzemer¹¹,
 N. Harnew⁵⁵, S.T. Harnew⁴⁶, J. Harrison⁵⁴, J. He³⁸, T. Head³⁹, V. Heijne⁴¹, K. Hennessy⁵²,
 P. Henrard⁵, L. Henry⁸, J.A. Hernando Morata³⁷, E. van Herwijnen³⁸, M. Heß⁶³, A. Hicheur²,
 D. Hill⁵⁵, M. Hoballah⁵, C. Hombach⁵⁴, W. Hulsbergen⁴¹, T. Humair⁵³, N. Hussain⁵⁵,
 D. Hutchcroft⁵², D. Hynds⁵¹, M. Idzik²⁷, P. Ilten⁵⁶, R. Jacobsson³⁸, A. Jaeger¹¹, J. Jalocha⁵⁵,
 E. Jans⁴¹, A. Jawahery⁵⁸, F. Jing³, M. John⁵⁵, D. Johnson³⁸, C.R. Jones⁴⁷, C. Joram³⁸,
 B. Jost³⁸, N. Jurik⁵⁹, S. Kandybei⁴³, W. Kanso⁶, M. Karacson³⁸, T.M. Karbach³⁸, S. Karodia⁵¹,
 M. Kelsey⁵⁹, I.R. Kenyon⁴⁵, M. Kenzie³⁸, T. Ketel⁴², B. Khanji^{20,38,k}, C. Khurewathanakul³⁹,
 S. Klaver⁵⁴, K. Klimaszewski²⁸, O. Kochebina⁷, M. Kolpin¹¹, I. Komarov³⁹, R.F. Koopman⁴²,
 P. Koppenburg^{41,38}, M. Korolev³², L. Kravchuk³³, K. Kreplin¹¹, M. Kreps⁴⁸, G. Krocker¹¹,
 P. Krokovny³⁴, F. Kruse⁹, W. Kucewicz^{26,o}, M. Kucharczyk²⁶, V. Kudryavtsev³⁴, K. Kurek²⁸,
 T. Kvaratskheliya³¹, V.N. La Thi³⁹, D. Lacarrere³⁸, G. Lafferty⁵⁴, A. Lai¹⁵, D. Lambert⁵⁰,
 R.W. Lambert⁴², G. Lanfranchi¹⁸, C. Langenbruch⁴⁸, B. Langhans³⁸, T. Latham⁴⁸,
 C. Lazzeroni⁴⁵, R. Le Gac⁶, J. van Leerdam⁴¹, J.-P. Lees⁴, R. Lefèvre⁵, A. Leflat³²,
 J. Lefrançois⁷, O. Leroy⁶, T. Lesiak²⁶, B. Leverington¹¹, Y. Li⁷, T. Likhomanenko⁶⁴, M. Liles⁵²,
 R. Lindner³⁸, C. Linn³⁸, F. Lionetto⁴⁰, B. Liu¹⁵, S. Lohn³⁸, I. Longstaff⁵¹, J.H. Lopes²,
 P. Lowdon⁴⁰, D. Lucchesi^{22,r}, H. Luo⁵⁰, A. Lupato²², E. Luppi^{16,f}, O. Lupton⁵⁵, F. Machefert⁷,
 F. Maciuc²⁹, O. Maev³⁰, S. Malde⁵⁵, A. Malinin⁶⁴, G. Manca^{15,e}, G. Mancinelli⁶, P. Manning⁵⁹,
 A. Mapelli³⁸, J. Maratas⁵, J.F. Marchand⁴, U. Marconi¹⁴, C. Marin Benito³⁶, P. Marino^{23,38,t},
 R. Märki³⁹, J. Marks¹¹, G. Martellotti²⁵, M. Martinelli³⁹, D. Martinez Santos⁴²,
 F. Martinez Vidal⁶⁶, D. Martins Tostes², A. Massafferri¹, R. Matev³⁸, A. Mathad⁴⁸, Z. Mathe³⁸,
 C. Matteuzzi²⁰, A. Mauri⁴⁰, B. Maurin³⁹, A. Mazurov⁴⁵, M. McCann⁵³, J. McCarthy⁴⁵,
 A. McNab⁵⁴, R. McNulty¹², B. Meadows⁵⁷, F. Meier⁹, M. Meissner¹¹, M. Merk⁴¹,
 D.A. Milanes⁶², M.-N. Minard⁴, D.S. Mitzel¹¹, J. Molina Rodriguez⁶⁰, S. Monteil⁵,
 M. Morandin²², P. Morawski²⁷, A. Mordà⁶, M.J. Morello^{23,t}, J. Moron²⁷, A.-B. Morris⁵⁰,
 R. Mountain⁵⁹, F. Muheim⁵⁰, K. Müller⁴⁰, M. Mussini¹⁴, B. Muster³⁹, P. Naik⁴⁶, T. Nakada³⁹,
 R. Nandakumar⁴⁹, I. Nasteva², M. Needham⁵⁰, N. Neri²¹, S. Neubert¹¹, N. Neufeld³⁸,
 M. Neuner¹¹, A.D. Nguyen³⁹, T.D. Nguyen³⁹, C. Nguyen-Mau^{39,q}, V. Niess⁵, R. Niet⁹,
 N. Nikitin³², T. Nikodem¹¹, A. Novoselov³⁵, D.P. O'Hanlon⁴⁸, A. Oblakowska-Mucha²⁷,
 V. Obraztsov³⁵, S. Ogilvy⁵¹, O. Okhrimenko⁴⁴, R. Oldeman^{15,e}, C.J.G. Onderwater⁶⁷,
 B. Osorio Rodrigues¹, J.M. Otalora Goicochea², A. Otto³⁸, P. Owen⁵³, A. Oyanguren⁶⁶,
 A. Palano^{13,c}, F. Palombo^{21,u}, M. Palutan¹⁸, J. Panman³⁸, A. Papanestis⁴⁹, M. Pappagallo⁵¹,
 L.L. Pappalardo^{16,f}, C. Parkes⁵⁴, G. Passaleva¹⁷, G.D. Patel⁵², M. Patel⁵³, C. Patrignani^{19,j},
 A. Pearce^{54,49}, A. Pellegrino⁴¹, G. Penso^{25,m}, M. Pepe Altarelli³⁸, S. Perazzini^{14,d}, P. Perret⁵,
 L. Pescatore⁴⁵, K. Petridis⁴⁶, A. Petrolini^{19,j}, E. Picatoste Olloqui³⁶, B. Pietrzyk⁴, T. Pilar⁴⁸,
 D. Pinci²⁵, A. Pistone¹⁹, S. Playfer⁵⁰, M. Plo Casasus³⁷, T. Poikela³⁸, F. Polci⁸,
 A. Poluektov^{48,34}, I. Polyakov³¹, E. Polcarpo², A. Popov³⁵, D. Popov¹⁰, B. Popovici²⁹,
 C. Potterat², E. Price⁴⁶, J.D. Price⁵², J. Prisciandaro³⁹, A. Pritchard⁵², C. Prouve⁴⁶,
 V. Pugatch⁴⁴, A. Puig Navarro³⁹, G. Punzi^{23,s}, W. Qian⁴, R. Quagliani^{7,46}, B. Rachwal²⁶,
 J.H. Rademacker⁴⁶, B. Rakotomiaramanana³⁹, M. Rama²³, M.S. Rangel², I. Raniuk⁴³,
 N. Rauschmayr³⁸, G. Raven⁴², F. Redi⁵³, S. Reichert⁵⁴, M.M. Reid⁴⁸, A.C. dos Reis¹,
 S. Ricciardi⁴⁹, S. Richards⁴⁶, M. Rihl³⁸, K. Rinnert⁵², V. Rives Molina³⁶, P. Robbe^{7,38},
 A.B. Rodrigues¹, E. Rodrigues⁵⁴, J.A. Rodriguez Lopez⁶², P. Rodriguez Perez⁵⁴, S. Roiser³⁸,
 V. Romanovsky³⁵, A. Romero Vidal³⁷, M. Rotondo²², J. Rouvinet³⁹, T. Ruf³⁸, H. Ruiz³⁶,
 P. Ruiz Valls⁶⁶, J.J. Saborido Silva³⁷, N. Sagidova³⁰, P. Sail⁵¹, B. Saitta^{15,e},
 V. Salustino Guimaraes², C. Sanchez Mayordomo⁶⁶, B. Sanmartin Sedes³⁷, R. Santacesaria²⁵,

C. Santamarina Rios³⁷, E. Santovetti^{24,l}, A. Sarti^{18,m}, C. Satriano^{25,n}, A. Satta²⁴,
D.M. Saunders⁴⁶, D. Savrina^{31,32}, M. Schiller³⁸, H. Schindler³⁸, M. Schlupp⁹, M. Schmelling¹⁰,
B. Schmidt³⁸, O. Schneider³⁹, A. Schopper³⁸, M.-H. Schune⁷, R. Schwemmer³⁸, B. Sciascia¹⁸,
A. Sciubba^{25,m}, A. Semennikov³¹, I. Sepp⁵³, N. Serra⁴⁰, J. Serrano⁶, L. Sestini²², P. Seyfert¹¹,
M. Shapkin³⁵, I. Shapoval^{16,43,f}, Y. Shcheglov³⁰, T. Shears⁵², L. Shekhtman³⁴, V. Shevchenko⁶⁴,
A. Shires⁹, R. Silva Coutinho⁴⁸, G. Simi²², M. Sirendi⁴⁷, N. Skidmore⁴⁶, I. Skillicorn⁵¹,
T. Skwarnicki⁵⁹, N.A. Smith⁵², E. Smith^{55,49}, E. Smith⁵³, J. Smith⁴⁷, M. Smith⁵⁴, H. Snoek⁴¹,
M.D. Sokoloff^{57,38}, F.J.P. Soler⁵¹, F. Soomro³⁹, D. Souza⁴⁶, B. Souza De Paula², B. Spaan⁹,
P. Spradlin⁵¹, S. Sridharan³⁸, F. Stagni³⁸, M. Stahl¹¹, S. Stahl³⁸, O. Steinkamp⁴⁰,
O. Stenyakin³⁵, F. Sterpka⁵⁹, S. Stevenson⁵⁵, S. Stoica²⁹, S. Stone⁵⁹, B. Storaci⁴⁰, S. Stracka^{23,t},
M. Straticiuc²⁹, U. Straumann⁴⁰, R. Stroili²², L. Sun⁵⁷, W. Sutcliffe⁵³, K. Swientek²⁷,
S. Swientek⁹, V. Syropoulos⁴², M. Szczekowski²⁸, P. Szczypka^{39,38}, T. Szumlak²⁷,
S. T'Jampens⁴, M. Teklishyn⁷, G. Tellarini^{16,f}, F. Teubert³⁸, C. Thomas⁵⁵, E. Thomas³⁸,
J. van Tilburg⁴¹, V. Tisserand⁴, M. Tobin³⁹, J. Todd⁵⁷, S. Tolk⁴², L. Tomassetti^{16,f},
D. Tonelli³⁸, S. Topp-Joergensen⁵⁵, N. Torr⁵⁵, E. Tournefier⁴, S. Tourneur³⁹, K. Trabelsi³⁹,
M.T. Tran³⁹, M. Tresch⁴⁰, A. Trisovic³⁸, A. Tsaregorodtsev⁶, P. Tsopelas⁴¹, N. Tuning^{41,38},
A. Ukleja²⁸, A. Ustyuzhanin⁶⁵, U. Uwer¹¹, C. Vacca^{15,e}, V. Vagnoni¹⁴, G. Valenti¹⁴, A. Vallier⁷,
R. Vazquez Gomez¹⁸, P. Vazquez Regueiro³⁷, C. Vázquez Sierra³⁷, S. Vecchi¹⁶, J.J. Velthuis⁴⁶,
M. Veltri^{17,h}, G. Veneziano³⁹, M. Vesterinen¹¹, J.V. Viana Barbosa³⁸, B. Viaud⁷, D. Vieira²,
M. Vieites Diaz³⁷, X. Vilasis-Cardona^{36,p}, A. Vollhardt⁴⁰, D. Volynskyy¹⁰, D. Voong⁴⁶,
A. Vorobyev³⁰, V. Vorobyev³⁴, C. Voß⁶³, J.A. de Vries⁴¹, R. Waldi⁶³, C. Wallace⁴⁸, R. Wallace¹²,
J. Walsh²³, S. Wandernoth¹¹, J. Wang⁵⁹, D.R. Ward⁴⁷, N.K. Watson⁴⁵, D. Websdale⁵³,
A. Weiden⁴⁰, M. Whitehead⁴⁸, D. Wiedner¹¹, G. Wilkinson^{55,38}, M. Wilkinson⁵⁹, M. Williams³⁸,
M.P. Williams⁴⁵, M. Williams⁵⁶, F.F. Wilson⁴⁹, J. Wimberley⁵⁸, J. Wishahi⁹, W. Wislicki²⁸,
M. Witek²⁶, G. Wormser⁷, S.A. Wotton⁴⁷, S. Wright⁴⁷, K. Wyllie³⁸, Y. Xie⁶¹, Z. Xu³⁹, Z. Yang³,
X. Yuan³⁴, O. Yushchenko³⁵, M. Zangoli¹⁴, M. Zavertyaev^{10,b}, L. Zhang³, Y. Zhang³,
A. Zhelezov¹¹, A. Zhokhov³¹, L. Zhong³.

¹ Centro Brasileiro de Pesquisas Físicas (CBPF), Rio de Janeiro, Brazil

² Universidade Federal do Rio de Janeiro (UFRJ), Rio de Janeiro, Brazil

³ Center for High Energy Physics, Tsinghua University, Beijing, China

⁴ LAPP, Université Savoie Mont-Blanc, CNRS/IN2P3, Annecy-Le-Vieux, France

⁵ Clermont Université, Université Blaise Pascal, CNRS/IN2P3, LPC, Clermont-Ferrand, France

⁶ CPPM, Aix-Marseille Université, CNRS/IN2P3, Marseille, France

⁷ LAL, Université Paris-Sud, CNRS/IN2P3, Orsay, France

⁸ LPNHE, Université Pierre et Marie Curie, Université Paris Diderot, CNRS/IN2P3, Paris, France

⁹ Fakultät Physik, Technische Universität Dortmund, Dortmund, Germany

¹⁰ Max-Planck-Institut für Kernphysik (MPIK), Heidelberg, Germany

¹¹ Physikalisches Institut, Ruprecht-Karls-Universität Heidelberg, Heidelberg, Germany

¹² School of Physics, University College Dublin, Dublin, Ireland

¹³ Sezione INFN di Bari, Bari, Italy

¹⁴ Sezione INFN di Bologna, Bologna, Italy

¹⁵ Sezione INFN di Cagliari, Cagliari, Italy

¹⁶ Sezione INFN di Ferrara, Ferrara, Italy

¹⁷ Sezione INFN di Firenze, Firenze, Italy

¹⁸ Laboratori Nazionali dell'INFN di Frascati, Frascati, Italy

¹⁹ Sezione INFN di Genova, Genova, Italy

²⁰ Sezione INFN di Milano Bicocca, Milano, Italy

²¹ Sezione INFN di Milano, Milano, Italy

- ²² *Sezione INFN di Padova, Padova, Italy*
- ²³ *Sezione INFN di Pisa, Pisa, Italy*
- ²⁴ *Sezione INFN di Roma Tor Vergata, Roma, Italy*
- ²⁵ *Sezione INFN di Roma La Sapienza, Roma, Italy*
- ²⁶ *Henryk Niewodniczanski Institute of Nuclear Physics Polish Academy of Sciences, Kraków, Poland*
- ²⁷ *AGH - University of Science and Technology, Faculty of Physics and Applied Computer Science, Kraków, Poland*
- ²⁸ *National Center for Nuclear Research (NCBJ), Warsaw, Poland*
- ²⁹ *Horia Hulubei National Institute of Physics and Nuclear Engineering, Bucharest-Magurele, Romania*
- ³⁰ *Petersburg Nuclear Physics Institute (PNPI), Gatchina, Russia*
- ³¹ *Institute of Theoretical and Experimental Physics (ITEP), Moscow, Russia*
- ³² *Institute of Nuclear Physics, Moscow State University (SINP MSU), Moscow, Russia*
- ³³ *Institute for Nuclear Research of the Russian Academy of Sciences (INR RAN), Moscow, Russia*
- ³⁴ *Budker Institute of Nuclear Physics (SB RAS) and Novosibirsk State University, Novosibirsk, Russia*
- ³⁵ *Institute for High Energy Physics (IHEP), Protvino, Russia*
- ³⁶ *Universitat de Barcelona, Barcelona, Spain*
- ³⁷ *Universidad de Santiago de Compostela, Santiago de Compostela, Spain*
- ³⁸ *European Organization for Nuclear Research (CERN), Geneva, Switzerland*
- ³⁹ *Ecole Polytechnique Fédérale de Lausanne (EPFL), Lausanne, Switzerland*
- ⁴⁰ *Physik-Institut, Universität Zürich, Zürich, Switzerland*
- ⁴¹ *Nikhef National Institute for Subatomic Physics, Amsterdam, The Netherlands*
- ⁴² *Nikhef National Institute for Subatomic Physics and VU University Amsterdam, Amsterdam, The Netherlands*
- ⁴³ *NSC Kharkiv Institute of Physics and Technology (NSC KIPT), Kharkiv, Ukraine*
- ⁴⁴ *Institute for Nuclear Research of the National Academy of Sciences (KINR), Kyiv, Ukraine*
- ⁴⁵ *University of Birmingham, Birmingham, United Kingdom*
- ⁴⁶ *H.H. Wills Physics Laboratory, University of Bristol, Bristol, United Kingdom*
- ⁴⁷ *Cavendish Laboratory, University of Cambridge, Cambridge, United Kingdom*
- ⁴⁸ *Department of Physics, University of Warwick, Coventry, United Kingdom*
- ⁴⁹ *STFC Rutherford Appleton Laboratory, Didcot, United Kingdom*
- ⁵⁰ *School of Physics and Astronomy, University of Edinburgh, Edinburgh, United Kingdom*
- ⁵¹ *School of Physics and Astronomy, University of Glasgow, Glasgow, United Kingdom*
- ⁵² *Oliver Lodge Laboratory, University of Liverpool, Liverpool, United Kingdom*
- ⁵³ *Imperial College London, London, United Kingdom*
- ⁵⁴ *School of Physics and Astronomy, University of Manchester, Manchester, United Kingdom*
- ⁵⁵ *Department of Physics, University of Oxford, Oxford, United Kingdom*
- ⁵⁶ *Massachusetts Institute of Technology, Cambridge, MA, United States*
- ⁵⁷ *University of Cincinnati, Cincinnati, OH, United States*
- ⁵⁸ *University of Maryland, College Park, MD, United States*
- ⁵⁹ *Syracuse University, Syracuse, NY, United States*
- ⁶⁰ *Pontifícia Universidade Católica do Rio de Janeiro (PUC-Rio), Rio de Janeiro, Brazil, associated to ²*
- ⁶¹ *Institute of Particle Physics, Central China Normal University, Wuhan, Hubei, China, associated to ³*
- ⁶² *Departamento de Física, Universidad Nacional de Colombia, Bogota, Colombia, associated to ⁸*
- ⁶³ *Institut für Physik, Universität Rostock, Rostock, Germany, associated to ¹¹*
- ⁶⁴ *National Research Centre Kurchatov Institute, Moscow, Russia, associated to ³¹*
- ⁶⁵ *Yandex School of Data Analysis, Moscow, Russia, associated to ³¹*
- ⁶⁶ *Instituto de Física Corpuscular (IFIC), Universitat de Valencia-CSIC, Valencia, Spain, associated to ³⁶*
- ⁶⁷ *Van Swinderen Institute, University of Groningen, Groningen, The Netherlands, associated to ⁴¹*

^a *Universidade Federal do Triângulo Mineiro (UFMT), Uberaba-MG, Brazil*

^b *P.N. Lebedev Physical Institute, Russian Academy of Science (LPI RAS), Moscow, Russia*

^c *Università di Bari, Bari, Italy*

- ^d *Università di Bologna, Bologna, Italy*
- ^e *Università di Cagliari, Cagliari, Italy*
- ^f *Università di Ferrara, Ferrara, Italy*
- ^g *Università di Firenze, Firenze, Italy*
- ^h *Università di Urbino, Urbino, Italy*
- ⁱ *Università di Modena e Reggio Emilia, Modena, Italy*
- ^j *Università di Genova, Genova, Italy*
- ^k *Università di Milano Bicocca, Milano, Italy*
- ^l *Università di Roma Tor Vergata, Roma, Italy*
- ^m *Università di Roma La Sapienza, Roma, Italy*
- ⁿ *Università della Basilicata, Potenza, Italy*
- ^o *AGH - University of Science and Technology, Faculty of Computer Science, Electronics and Telecommunications, Kraków, Poland*
- ^p *LIFAELS, La Salle, Universitat Ramon Llull, Barcelona, Spain*
- ^q *Hanoi University of Science, Hanoi, Viet Nam*
- ^r *Università di Padova, Padova, Italy*
- ^s *Università di Pisa, Pisa, Italy*
- ^t *Scuola Normale Superiore, Pisa, Italy*
- ^u *Università degli Studi di Milano, Milano, Italy*
- ^v *Politecnico di Milano, Milano, Italy*